Role of mineralogy in controlling fracture formation

by

Olivia Brunhoeber

A thesis submitted to the Graduate Faculty of
Auburn University
in partial fulfillment of the
requirements for the Degree of
Master of Civil & Environmental Engineering

Auburn, Alabama
May 1, 2021

Keywords: Fracture, mineralogy, shale, caprock

Approved by

Lauren E. Beckingham, Chair, Assistant Professor of Civil & Environmental Engineering
Jack Montgomery, Assistant Professor of Civil & Environmental Engineering
Mark Barnett, Professor of Civil & Environmental Engineering

Abstract

Geologic CO_2 storage systems rely on impermeable caprock layers to prevent fluid leakage and maintain system integrity. In these systems, mineral dissolution and precipitation reactions controlled by the reactivity of the accessible mineralogy can alter formation porosity and permeability over time. In the case of fractures, mineralogy that may otherwise be inaccessible can be exposed at the fracture surface. CO_2-brine-mineral interactions at the fracture surface control the potential for CO_2 leakage where reactions may increase or decrease fracture permeability, promoting or inhibiting leakage. Therefore, predicting the mineralogy that is likely to be present at the fracture surface will aid in understanding how the fracture will evolve. Here, shale samples taken from the Mancos formation (western United States) and the Marcellus formation (northeastern United States) are mechanically fractured via unconfined compression. The fractured surfaces are examined using scanning electron microscopy (SEM) energy dispersive spectroscopy (EDS) to create quantifiable mineral maps representative of fracture surfaces. This process is repeated on thin sections of the same cores to analyze near fracture rock matrices both parallel and perpendicular to the fracture. The remaining sample is used for x-ray powder diffraction (XRD) to determine the mineralogy of the bulk sample. After fracturing, the Mancos sample had two visually distinct lithofacies present at the fracture surface that were quantified using optical microscopy. Two mineral maps of each Mancos lithofacies showed the light layer is made up of quartz (25-40%), calcite (22%), and clay (27-48%), and the dark layer is rich in clay (71-79%). The matrices parallel and perpendicular to the fracture are comprised of 6 and 10% calcite, 39 and 44% quartz, and 45 and 27% clay, respectively. Compared to the XRD and matrix data, the dark lithofacies that makes up 71% of the fracture surface is high in clay content and low in quartz content. The light lithofacies that makes up 29% of the surface is slightly low in quartz and high in calcite

2

content. As a result, for the Mancos sample, the fracture surface has relatively high clay content suggesting the fracture formed predominately through weak mineral phases. In contrast to this, the Marcellus results show the mineralogy of the fracture surface, matrix, and bulk sample as over 94% calcite. Because the Mancos sample showed interesting results, the mineral maps were further analyzed using autocorrelation to quantify the mineral distributions at the fracture surface and matrices. From this we have found that the induced fracture formed within a clay rich region about 400 microns thick. In this region, clay is more likely than quartz or carbonate to occur near the fracture, with the probability of occurrence decreasing as distance from the fracture increases. When comparing the fracture surface and matrix mineralogies, we see that the fracture surface mineralogy has a more uniform distribution at all distances.

Acknowledgments

I wish to express my sincerest gratitude to Dr. Lauren Beckingham for her guidance and support throughout this project. I am thankful for the opportunity she provided me to grow in this field of expertise. I would like to thank my committee members Dr. Jack Montgomery and Dr. Mark Barnett for their wonderful feedback and assistance. I would like to extend a special thanks to Dr. Lawrence Anovitz for helping me create and understand the autocorrelation section of this work. It would not have been possible without you.

My warmest thanks go to Fanqi Qin and Chidera Iloejesi for their support and encouragement throughout this journey. I also wish to thank Parisa Asadi and Fahim Salek for their helpful advice and support. These thanks extend to all of the WRISES group members for their excellent feedback and consistent support. It has been a pleasure to be a part of such a welcoming and supportive group.

Lastly, I wish to thank my family. My father, brother, and sister for their love and support throughout all of my decisions. My fiancé for his consistent love and encouragement. And my mother for providing me with a belief that anything is possible.

Table of Contents

List of Tables

List of Figures

List of Abbreviations

CCS   Carbon capture and storage

COD   Crystallography open database

EDS   Energy dispersive spectroscopy

QCC   Quartz, calcite, and clay

RIR   Relative intensity ratio

SEM   Scanning electron microscopy

XRD   X-ray powder diffraction

Chapter 1

Introduction

1.1 Motivation

Since the 1970s scientists have known that the release of certain gases like carbon dioxide (CO_2), methane (CH_4), and nitrous oxide (N_2O) can trap heat in the atmosphere creating a greenhouse effect (Hansen, et al. 1998). Though a certain concentration of greenhouse gas (GHG) is necessary for a habitable environment, the surge of emissions brought on by the industrial revolution of the mid-18th century has propelled CO_2, CH_4, and N_2O concentrations to 35%, 142%, and 18% increases in 2005 from preindustrial levels (IPCC, 2007). To mitigate the most damaging effects of climate change, the Intergovernmental Panel on Climate Change (IPCC) has determined that the average global temperature rise must be kept within 2°C compared with that of pre-industrial times (IPCC, 2014). Already, however, sea levels are anticipated to rise 32-90 mm by 2100, with some studies estimating a minimum rise of 75mm, through melting of the Greenland ice sheet alone (Goelzer, et al. 2020; Gillet-Chaulet, et al. 2012). This rise, along with increasingly intense drought and severe weather, will contribute to the creation of 200 million environmental refugees by 2050 (Biermann & Boas, 2008; Myers, 2002).

Minimizing climate change impacts from this point forward will require unprecedented technological and institutional changes as emissions are primarily a result of fossil fuel use, land use change, and agriculture (IPCC, 2007). Unfortunately, despite an increasing number of mitigation policies GHG concentrations are still rising (IPCC, 2014). As a result, unconventional engineering solutions are expected to play a role in minimizing atmospheric GHG concentrations. One of these solutions is carbon capture and storage (CCS) (IPCC, 2005; Yu, et al. 2008). Here, CO_2 is collected from industrial sources, compressed, and transported to a selected geological

storage site where it is injected into a deep formation reservoir for long-term storage. This long-term storage is the result of CO_2 mixing with existing brine formation, creating low-pH conditions favorable for calcium carbonate precipitation ($CaCO_3$), effectively sequestering CO_2 that would otherwise be released in the atmosphere (Oelkers et al., 2008). As a result, the formation selected for injection plays a critical role in trapping results, where some criteria for selection includes reservoir permeability and mineral composition, the presence of a vertically sealing caprock, and the absence of faults and fracture networks (Miocic, et al. 2016; Watson, et al. 2005)

1.2 Role of mineralogy in controlling fracture formation

In subsurface systems like CCS, fluid-rock interactions have the potential to alter formation porosity and permeability through the dissolution and precipitation of minerals (Tian, et al. 2019; Fitts and Peters, 2013; Bensinger and Beckingham 2020; Sabo and Beckingham 2021). These reactions are controlled by the accessibility of mineral surfaces to the formation fluid, however, estimated mineralogy of the bulk formation does not necessarily represent the accessible mineralogy due to disconnected pores or clay coatings (Peters 2009, Landrot et al. 2012, Beckingham et al. 2016). This misrepresentation of controlling mineralogy is also likely to be true in the case of fractures, the presence of which can impact system integrity by creating high flow conduits for injected fluid (Ellis, et al. 2011; Major, et al. 2018; Fitts, et al. 2012). Because supercritical CO_2 is less dense than existing formation fluid, it can migrate upward into caprock fractures interacting with exposed mineralogy (Singh et al., 2019). The evolution of fracture aperture and permeability over time is greatly dependent upon the mineral distribution at the fracture surfaces, where unreactive lamination can inhibit fluid flow (Spokas, et al. 2018), and

highly reactive surfaces with little to no lamination can create many flow channels unlikely to seal (Deng, et al. 2015; Jones and Detwiler, 2016; Spokas, et al. 2018).

Though evidence of mineralogy impacting fracture evolution is strong, links to mineralogy and fracture formation are not. It is widely accepted that rock composition plays a role in fracture development (Guo, et al. 2015; Tian and Daigle, 2019; Ding, et al. 2012; Yoon, et al. 2019; Gale, et al. 2014; Na, et al. 2017), however, little data exists on what minerals can be expected along the fracture walls, ultimately influencing conductivity over time. Tian and Daigle (2019) found that microfractures are more likely to form within organic matter. For larger fractures, Yoon et al. (2019) examined thin sections of fractures formed by confined compression testing and found that the fracture propagated between quartz grains, within clay layers. From this we can hypothesize that fractures will follow a path of least resistance, passing through weak mineral phases (clay, organic matter) instead of hard ones (quartz, feldspar). Though fracture formation has been examined in the context of rock mechanical properties (i.e. brittleness/ductility, Young's Modulus) (i.e. Holt, et al. 2015; Gale, et al. 2014, Brunhoeber, et al. 2020), it is a challenge to interpret how they relate to specific minerals whose properties are examined differently (i.e. Moh's scale of mineral hardness). Therefore, in this work, we seek to understand what role mineralogy plays in controlling fracture formation by examining the mineral abundance present at a fractures surface compared to that of the bulk sample. With this information we hope to enhance the understanding of how fracture surface composition may vary with respect to the surrounding rock matrix and make implications on how this might impact evolution in reactive systems.

1.3 Analysis of mineralogical spatial variation through autocorrelation

In addition to abundance, mineral distribution greatly impacts reactive fracture evolution and sealing capacity in caprocks (Deng, et al. 2015; Spokas, et al. 2018; Jones and Detwiler, 2016). As such, there is a need to quantitatively describe mineral spatial distributions. A variety of ways exist in the literature for this, including variograms, entrograms, and autocorrelation. All three methods create graphs in a similar way by measuring some degree of variability, randomness, or correlation in a dataset over distance (i.e., Gringarten & Deutsch, 2001; Bianchi & Pedretti, 2018; Berryman & Blair, 1986). For all methods it is assumed that at some distance the distribution of the dataset will become random where within this distance heterogeneities will hold some relationship to each other. By applying any of these methods, we assume that the dataset being analyzed has some degree of spatial dependence, such that points in close proximity are more alike than points farther away (i.e., topography, hydraulic conductivity). In mineral distributions, we can expect that randomness will occur just beyond the grain size of the mineral being evaluated. For our purposes, a two-point autocorrelation analysis was chosen to be performed on different areas of the same shale sample. The autocorrelation method was chosen for its ability to perform cross-correlation, or to evaluate two parameters (mineral phases) with respect to each other (Anovitz, et al. 2021). This work will build off the imaging results in Chapter 2 by analyzing mineral distributions of the fracture surfaces compared with that of the matrix, and the relationship between the fracture surface and different mineral phases just beyond it.

1.4 Objectives

The objective of this study is to determine if a relationship exists between fracture formation and rock mineralogy to ultimately improve predictions of reactive fracture evolution in

subsurface CO_2 utilization and storage systems. The approach will be to quantify mineral abundance and distribution on fracture surfaces and in the unfractured matrix of shale samples. By comparing mineralogies at the fracture surface with that of the surrounding matrix and bulk sample we may observe disparities and establish a basis for what may define such a relationship. If no discrepancies in abundance are observed, it will be reasonable to assume that bulk mineralogy accurately reflects that of the fracture surface, where subsequent geochemical reactions will be strictly a matter of mineral distribution (i.e., Spokas, et al. 2018). Should discrepancies in mineral abundance at the surface be observed, this may indicate that fracture mineralogy and subsequent geochemical reactivity is unique as compared to the rest of the formation. This is the first study to consider the role of mineralogy in controlling fracture formation and the subsequent composition and distribution of minerals on fracture surfaces. As such, results from this study will indicate if a fracture-mineral relationship may exist and lay groundwork for future studies.

Chapter 2

Role of mineralogy in controlling fracture formation

Olivia M. Brunhoeber[1], Lawrence M. Anovitz[2], Lauren E. Beckingham[1]*

[1]*Department of Civil & Environmental Engineering, Auburn University, Auburn 36849*

[2] *Chemical Sciences Division, MS 6110, Oak Ridge National Laboratory, Oak Ridge, TN 37831*

* Corresponding author: leb@auburn.edu

Manuscript in preparation.

2.1 Abstract

Subsurface systems like CO_2 sequestration rely on impermeable caprocks for safe storage to maintain pressure and prevent leakage of the injected CO_2. The presence of fractures in caprocks can threaten system integrity by introducing high permeability flow paths. In reactive systems like this, rock mineralogy controls precipitation and dissolution reactions, altering the porosity and permeability of the formation. With the existence of fractures, minerals that are otherwise inaccessible can become exposed to the injected fluid, resulting in reactions differing from those predicted leveraging bulk formation mineralogy data. This work seeks to understand the relationship between mineralogy and fracture formation by evaluating the minerals present at the fracture, within the near fracture matrix, and within the bulk sample. Here, core samples from the Mancos and Marcellus formations are mechanically fractured via unconfined compression. The fracture surfaces and near fracture matrices of each sample are analyzed using scanning electron microscopy (SEM) energy dispersive spectroscopy (EDS) to quantify the surface mineralogies. X-ray powder diffraction (XRD) data of the same core samples show the Mancos formation contains 52% quartz, 19% clay, and 8% calcite and the Marcellus formation contains over 96% calcite. For the Mancos sample, 79% of the fracture surface is comprised of a dark, clay-rich lithofacies (71 to

80% clay) with the remaining 21% comprised of a light, quartz-calcite-clay lithofacies (27 to 49% clay, 25 to 40% quartz, 22% calcite). Though the Mancos matrix also shows slightly high clay content compared to XRD (up to 35%), the combined results suggest that the fracture formed predominately in clay-rich lithofacies and along clay-clay mineral interfaces. Due to the high calcite content in the Marcellus sample, little discrepancies are found between the bulk, matrix, and surface mineralogies, likely due to the homogeneity of this sample.

2.2 Introduction

In subsurface CO_2 systems, impermeable caprocks are necessary to prevent fluid migration and leakage. However, the presence of fractures and the evolution of reactive fractures over time can pose increased risk to system integrity (Ellis, et al. 2011; Major, et al. 2018; Fitts, et al. 2012). It is well understood that mineral dissolution and precipitation reactions can alter formation porosity and permeability (Tian, et al. 2019; Fitts and Peters, 2013; Bensinger and Beckingham 2020; Sabo and Beckingham 2021). When considering these reactions in fractures, it is not well understood if fracture permeabilities will be enhanced by dissolution of minerals on the fracture surfaces (Ellis, et al. 2011) or reduced due to cementation from mineral precipitation (Gutierrez, et al. 2000). The formation of preferential flow channels is a common occurrence in fractures (Deng, et al. 2015; Spokas, et al. 2018), where the spatial distribution of mineral heterogeneities can both prevent (Spokas, et al. 2018) and promote (Jones and Detwiler, 2016) channelization. However, the distribution of minerals at the fracture surface, and the impact on sealing capacity, is not well understood.

When considering fracture development, it is clear that rock composition plays a critical role (Guo, et al. 2015; Tian and Daigle, 2019; Ding, et al. 2012; Yoon, et al. 2019; Gale, et al. 2014). This role is most often discussed in terms of rock mechanics including Young's Modulus,

Poisson's ratio, and brittleness/ductility indices. Rocks containing high proportions of brittle minerals (silica, feldspar, carbonate), though harder to deform, tend to produce many highly conductive fractures (i.e., Ding et al. 2012). In contrast, weaker rocks with higher ductile mineral content (organic matter, clay) are more prone to the formation of microfractures within the weak mineral phases (i.e., Laubach, et al. 2009). It should be noted here, however, that the quantification of brittleness is not always consistent (Holt, et al. 2015), and porosity, grain size, and confining stress can also influence deformation (Holt, et al. 2015; Gale, et al. 2014; Zhang, et al. 2016).

Where fractures form in regard to different mineral phases and individual mineral grains is important for assessing reactivity but has largely not been considered. From the observations of bulk rocks (particularly Yoon, et al. 2019), one could hypothesize that fractures will form within soft, ductile minerals (clay, organic matter) as opposed to hard, brittle minerals (quartz, carbonate). However, a gap exists between the mechanical properties of rock samples and individual mineral phases. When considering the strengths of individual mineral phases, Moh's scale of mineral hardness is the most common method. This, however, may not accurately assess the behavior of phases in the bulk sample and cannot account for mineral boundaries. In this work, we consider the distribution of minerals on fracture surfaces in hopes to enhance understanding of the role of mineralogy in controlling fracture formation to improve predictive capabilities of reactive fracture evolution and implications for subsurface CO_2 systems.

2.3 Materials and Methodology

2.3.1 Samples and Sample Preparation

1" by 2" shale cores from the Mancos formation, found in the Western United States, and the Marcellus formation, found in the Mid-western and North-eastern United States, are used in this work. Four samples from each formation were fractured by applying unconfined uniaxial compressive stress to create initial fracture surfaces for analyzing. Prior to loading, the edges of each core were sanded level to prevent any influence of point loading. Each shale core was loaded at a rate of 0.5 mm/minute until an initial fracture was formed. Similar fracture results were found for multiple samples, where two Marcellus cores fractured smoothly down the middle, and three Mancos cores fractured relatively straight along the edge. One sample per formation was then selected for imaging analysis based on the suitability of the fracture surface for imaging (Fig. 2.1).

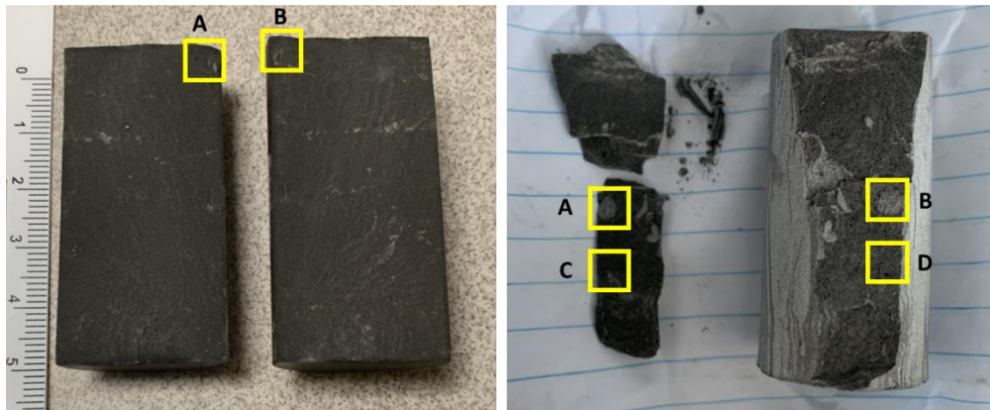**Figure 2.1.** Photo marking locations of SEM-EDS images on the induced fracture surfaces for Marcellus (left) and Mancos (right).

2.3.3 Surface Imaging

The fracture surfaces were imaged using SEM EDS imaging. Images were captured at aligning points on the fracture surfaces. The Mancos shale had two distinct strata of noticeably different compositions based on color (light/dark) and a set of correlating images were taken in

each region. Optical microscopy was used to take magnified images of the entire Mancos fracture surface to quantify the amount of the two strata (Fig. 2.2). The fracture surfaces and corresponding image locations for each sample are shown in Fig. 2.1.

Quantitative image processing using MATLAB and ImageJ was carried out on SEM and optical images to determine mineral and strata volume fractions. Minerals were identified through analysis of EDS elemental maps informed with mineralogy from XRD analysis. Binary images representing individual elements were created by manually applying mean filters and thresholding EDS images in ImageJ to establish solid grains, followed by processing in MATLAB to remove residual noise pixels. Mineral phases were identified based on their ideal chemical composition by evaluating the elements present at each pixel. Using this logic, mineral maps were created in MATLAB by assigning a unique color to each phase and assigning a mineral phase to each pixel. Volume fractions of each mineral were then quantified by pixel counting. A representative elemental volume analysis (Appendix A) was carried out on the processed images to ensure that the areas analyzed were representative of the sample. The mineralogy of the fracture interface was then considered by comparison of mineralogy at adjoining points on the fracture surfaces. Both the optical surface images and SEM mineral map pairs were compared in MATLAB, pixel by pixel, to determine the composition of the mineral interface on each side of the fracture.

2.3.4 Matrix Imaging

Once surface imaging was complete, thin sections of the sample adjacent and perpendicular to the fracture were created for additional SEM imaging (example given in Appendix A, Figure A.3). The fractured core samples were first adjoined using epoxy before sending cured samples to Applied Petrographic Services Inc. for thin section preparation. The resulting thin sections were

20

imaged and processed using the same techniques as above to determine the mineral distribution of the near fracture rock matrix both perpendicular and parallel to the induced fracture.

2.4 Results and Discussion

2.4.1 XRD

Collected XRD spectra and results of the peak matching in DIFFRAC.EVA are shown in Figure 2.2 for the Mancos sample and Figure 2.3 for the Marcellus sample. Using the specific gravity of each mineral, the percent of each mineral by weight from the software was translated into mineral percent by volume for easy comparison with the imaging analysis data. These values are given in Table 2.1 for both the Mancos and Marcellus samples. The Mancos sample is comprised of 52.1% quartz, ~8% illite, albite, and calcite, followed by 7.2% muscovite, 6.7% K-feldspar, 6.6% dolomite, 3.2% kaolinite, and 0.1% pyrite. The Marcellus sample is 96.7% calcite, with 3% quartz and 0.3% pyrite.

Table 2.1. XRD results of the Mancos and Marcellus samples given as percent volume.

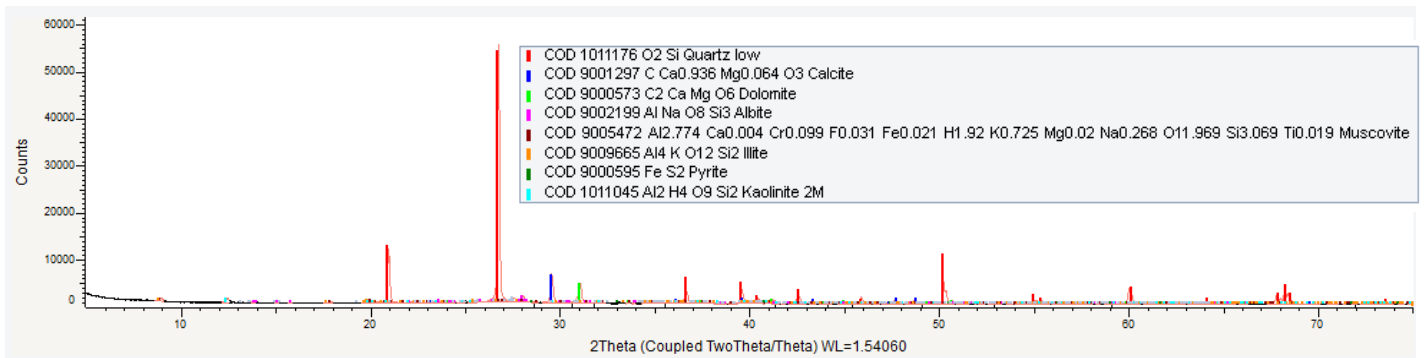|	Muscovite	Kaolinite	Illite	K-feldspar	Albite	Quartz	Pyrite	Calcite	Dolomite
Mancos	7.2	3.2	8.1	6.7	8.0	52.1	0.1	8.0	6.6
Marcellus	-	-	-	-	-	3.0	0.3	96.7	-

Figure 2.2. Data peaks with assigned minerals shown as colored lines for the Mancos sample.
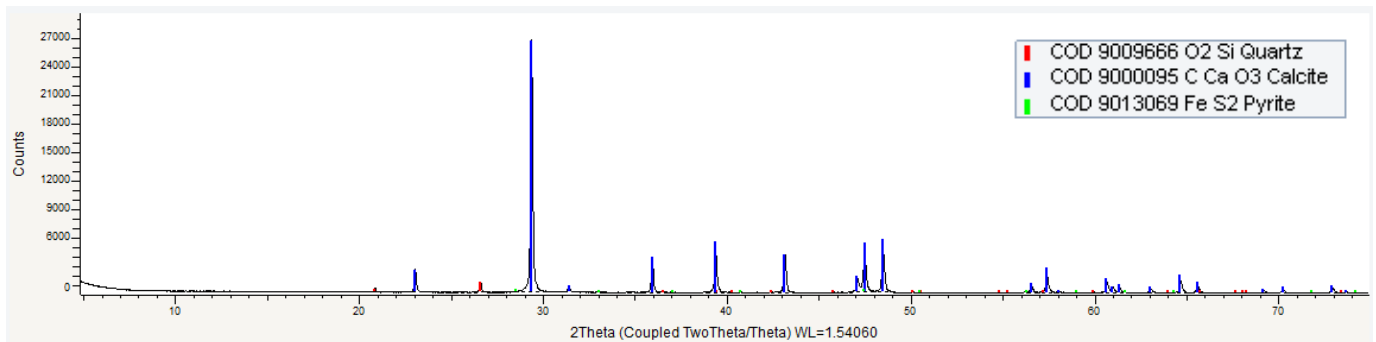

Figure 2.3. Data peaks with assigned minerals shown as colored lines for the Marcellus sample.

2.4.2 Imaging Analysis of Mancos Shale

Optical images of the induced fracture surfaces and the respective processed SEM-EDS mineral maps for the Mancos sample are shown in Figures 2.4 and 2.5. From the optical images we can determine that 71% of the fracture surface is made up of the darker facies, and 29% is made of the lighter facies. To better understand and categorize these layers, the mineralogy of each facies is quantified from the respective SEM mineral maps where the resulting data is given in Table 2.2. From this data, we see that the dark Mancos facies is rich in clay as compared to the lighter facies that has more equal amounts of quartz, clay, and calcite, and will therefore be referred to as the QCC layer. It should be noted for this sample that the term

Figure 2.4. Optical microscopy images of the induced fracture surface showing locations of SEM-EDS images, where areas A and B correspond the lighter facies and C and D to the darker facies.

"clay" may include kaolinite, illite/smectite, and/or muscovite. Though identified when possible, similarities in chemical formulas and challenges in image and XRD processing contribute to uncertainties in discerning discrete clay phases.
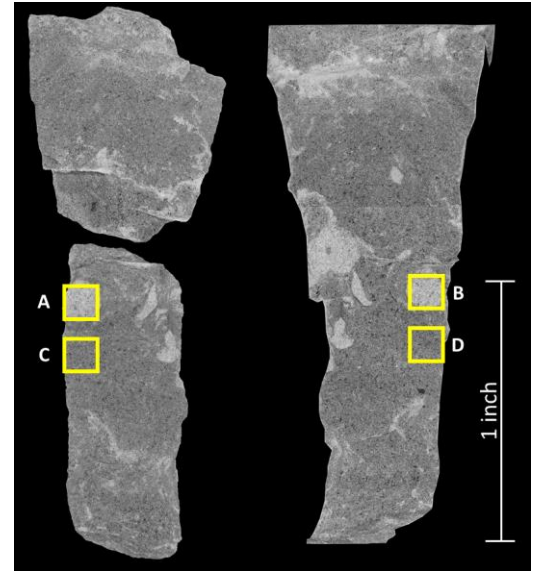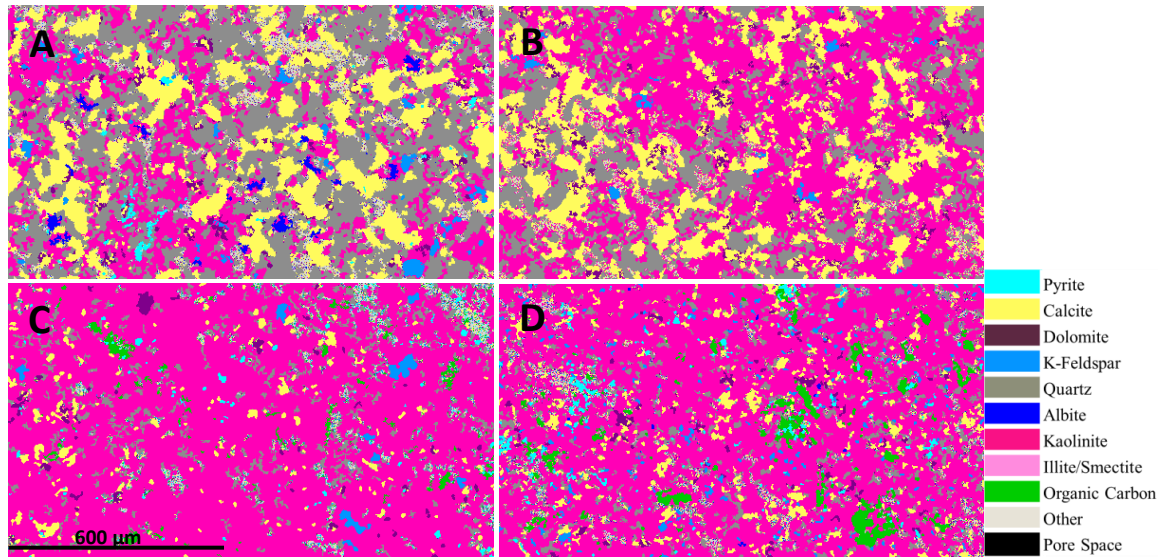
Figure 2.5. Processed SEM-EDS mineral maps of the fracture surface. A and B correspond to the QCC (light) facies (Fig. 2.4) which and is predominately comprised of quartz (dark gray), calcite (yellow), and clay (kaolinite as dark pink and illite/smectite as light pink), with minor phases including dolomite (purple), pyrite (cyan), albite (dark blue), K-feldspar or muscovite (light blue), carbon (green), and other (light gray). C and D correspond to the clay (dark) facies, predominately comprised of kaolinite (pink).

Table 2.2. Fracture surface (Fig. 2.5) and matrix (Fig. 2.6) mineralogy as volume percentages determined from pixel counting for Mancos shale.

Mineral	A (v%)	B (v%)	C (v%)	D (v%)	Perpendicular to fracture (v%)	Parallel to fracture (v%)
Pyrite	0.68	-	1.29	2.09	2.20	0.11
Calcite	22.25	21.87	3.64	6.79	9.79	5.67
Dolomite	2.49	2.06	1.53	2.16	5.67	6.08
K-Feldspar	1.81	0.72	1.51	2.33	1.65	2.05
Quartz	40.03	25.12	8.49	9.59	44.18	38.66
Albite	1.45	-	-	0.24	1.28	1.10
Kaolinite	26.67	48.47	79.71	71.03	8.45	10.27
Illite/Smectite	-	-	-	-	18.59	34.68
Organic Carbon	-	-	1.92	4.05	2.08	1.05
Other	4.62	1.76	1.92	1.72	1.13	0.33
Pore Space	-	-	-	-	4.98	-

The composition of the fracture interface is given in Tables 2.3 and 2.4 where columns represent the mineralogy of one image (fracture surface), and rows represent the mineralogy of its adjacent image (opposite fracture surface). The intersection of column mineral i and row mineral j represents the percentage of the fracture surface that occurred at an i-j interface. From analysis of the optical images (Fig. 2.4), we find that the fracture surface predominantly occurs at interfaces comprised of clay-clay facies (72% clay-clay facies, 9% QCC-QCC facies, and 19% clay-QCC facies). In terms of individual mineral phases in the QCC (light) facies (Table 2.3), 26% of the fracture interface is at a quartz-kaolinite interface, followed by 17% calcite-kaolinite, 15% quartz-calcite, 13% kaolinite-kaolinite, and 10% quartz-quartz. For the clay (dark) facies (Table 2.4), the fracture interface is predominately kaolinite-kaolinite (56%), followed by quartz-kaolinite (14%). For both lithofacies, quartz-kaolinite and kaolinite-kaolinite are prominent mineral interfaces for fracture, though mineral contents at each surface play a significant role in determining the percentage of each interface.

Table 2.3. Fracture interface data for QCC (light) Mancos areas where columns represent the mineralogy of image A as percent volume and rows represent the mineralogy of the adjacent image B as percent volume.

	Quartz	Calcite	Dolomite	K-spar	Kaolinite	Other	B (total)
Quartz	9.515	8.956	0.944	0.301	19.628	0.688	40.032
Calcite	5.697	4.751	0.374	0.128	10.897	0.406	22.253
Dolomite	0.573	0.508	0.042	0.025	1.291	0.048	2.487
Pyrite	0.174	0.163	0.014	0.003	0.313	0.014	0.682
K-spar	0.675	0.354	0.030	0.000	0.718	0.035	1.811
Kaolinite	6.859	5.877	0.564	0.227	12.681	0.458	26.666
Albite	0.461	0.304	0.029	0.003	0.631	0.026	1.453
Other	1.164	0.960	0.068	0.029	2.311	0.085	4.616
A (total)	25.119	21.873	2.064	0.715	48.469	1.760	

Table 2.4. Fracture interface data for clay (dark) Mancos areas where columns represent the mineralogy of image C as percent volume and rows represent the mineralogy of the adjacent image D as percent volume.

	Quartz	Calcite	Dolomite	Pyrite	K-spar	Kaolinite	Albite	Carbon	Other	D (total)
Quartz	0.817	0.568	0.168	0.173	0.174	6.153	0.016	0.290	0.130	8.489
Calcite	0.401	0.223	0.065	0.105	0.074	2.556	0.016	0.130	0.072	3.642
Dolomite	0.157	0.106	0.022	0.028	0.058	1.092	0.001	0.041	0.020	1.526
Pyrite	0.107	0.097	0.016	0.022	0.029	0.928	0.004	0.063	0.027	1.294
K-spar	0.162	0.098	0.052	0.028	0.018	1.038	0.003	0.071	0.035	1.506
Kaolinite	7.625	5.427	1.779	1.662	1.881	56.504	0.193	3.269	1.371	79.710
Carbon	0.163	0.138	0.027	0.048	0.040	1.331	0.001	0.141	0.029	1.919
Other	0.155	0.134	0.027	0.026	0.054	1.428	0.006	0.050	0.035	1.915
C (total)	9.586	6.792	2.157	2.091	2.328	71.031	0.242	4.054	1.720	

Mineral maps of the near fracture matrix are shown in Figure 2.6. The matrix is dominated by quartz (39-44%) and clay (27-45%) mineral phases (Table 2.2). It should be noted that this is a relatively higher clay content than determined via XRD for the bulk sample (11.4% clay). This is likely due to natural variations in the sample composition where samples from the same core sample were used for XRD and imaging analyses. When compared to the average mineralogy of the fracture surface (Tables 2.1 and 2.2) it is evident that the matrix has a significantly higher quartz content, suggesting the fracture preferentially formed at clay-clay interfaces. Tian and Daigle (2019) found that 90% of microfractures formed within clay or organic matter, often along quartz or carbonate grain boundaries. Yoon et al. (2019), examined the cross-section of a Mancos shale fracture formed by compression with confining stress loaded parallel and perpendicular to bedding and found that fractures formed within more clay-rich micro-lithofacies, propagating between quartz grains. These observations agree with those of this work where clay is more prevalent on the fracture surface than is expected from the bulk mineralogy. This may suggest that fracture formation is governed by the relative strength of the mineral phases where clay minerals are weaker in comparison to quartz.
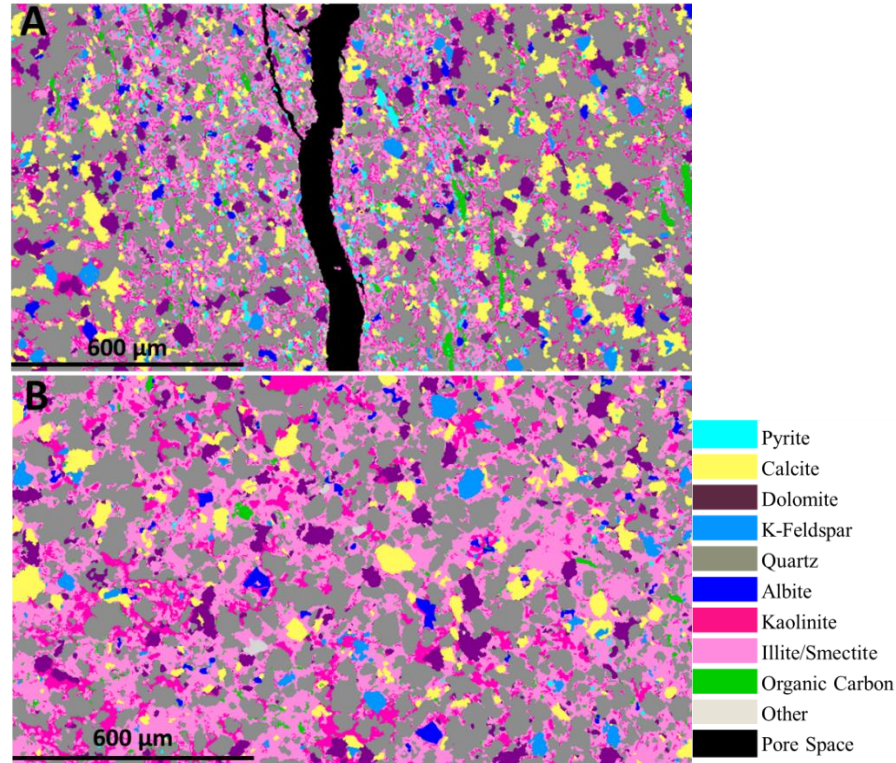
Figure 2.6. Processed SEM-EDS mineral maps of the near fracture matrix via thin sections. A shows the matrix perpendicular to the imaged fracture surface where the fracture shown is the fracture imaged in Fig. 2.5, and B shows the matrix parallel to that fracture.

2.4.3 Imaging Analysis of Marcellus Shale

Processed mineral maps for the Marcellus fracture surface and matrix are shown in Fig. 2.7 and 2.8 respectively. The mineral contents at all four of the locations shown are consistent with that of the bulk XRD (Table 2.5). This sample is relatively homogeneous such that the bulk sample, fracture surface, and nearby matrix mineralogies are all comprised of more than 95% calcite. As a result, the fracture interface is dominated (94%) by calcite-calcite pixels (Table 2.6). The presence of clay in the mineral maps, and its absence in the XRD data, suggests clay content in the bulk sample is less than the 5% threshold needed to be distinguishable in XRD. Processed mineral maps reveal clay minerals present as filling in preexisting fractures, as evident in the longitudinal matrix in Fig. 2.8B.
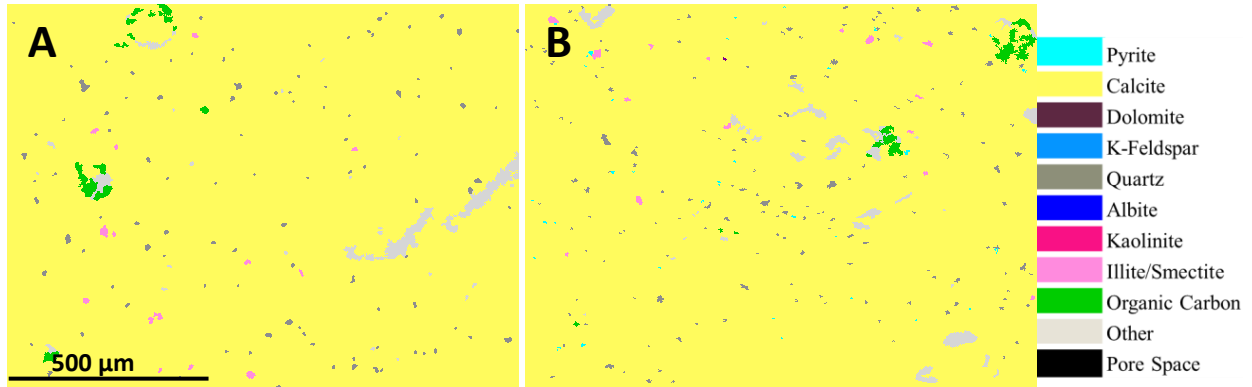
Figure 2.7. Processed SEM-EDS mineral maps of the Marcellus shale fracture surface, where A and B correlate to which side of the fracture the image is from (Figure 2.1).
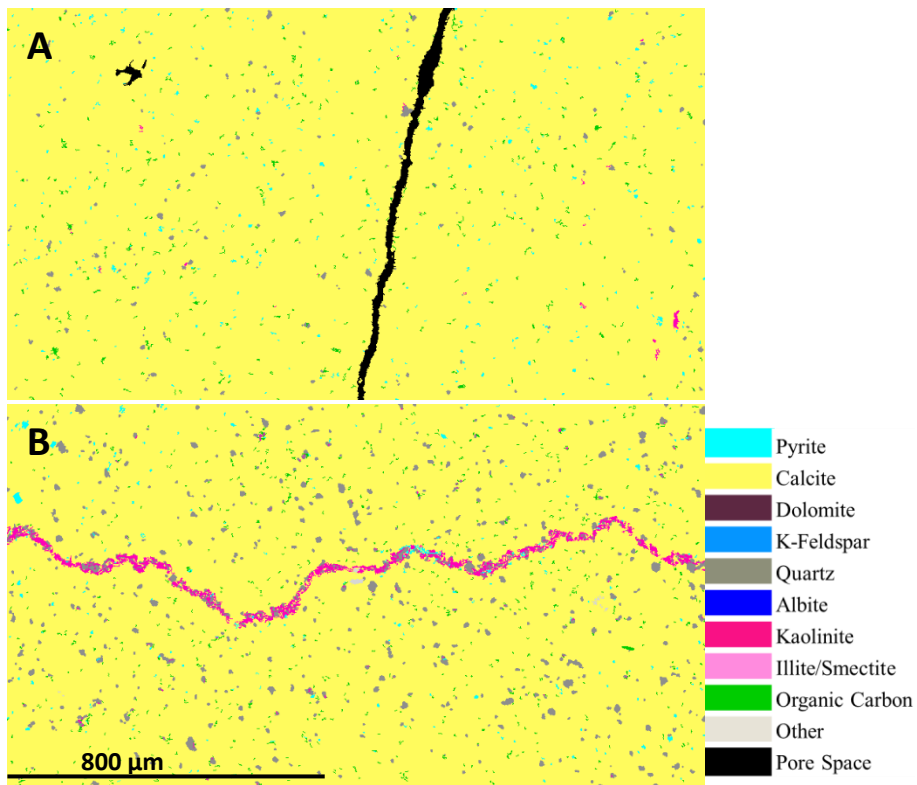

Figure 2.8. Processed SEM-EDS mineral maps of the near fracture matrix. A shows the matrix perpendicular to the imaged fracture surface. B shows the matrix parallel to the imaged fracture, giving an example of a pre-existing clay filled fracture.

Table 2.5. Fracture surface (A and B) and matrix mineralogy as volume percentages determined by pixel counting compared for Marcellus shale.

Mineral	A (v%)	B (v%)	Perpendicular to fracture (v%)	Parallel to fracture (v%)
Pyrite	0.098	-	0.532	0.427
Calcite	96.969	97.135	98.090	93.928
Dolomite	0.007	-	-	-
Quartz	0.733	0.680	0.559	3.355
Kaolinite	0.219	0.213	0.069	1.389
Organic Carbon	0.561	0.557	0.750	0.855
Other (Al only)	1.414	1.414	-	0.046

Table 2.6. Fracture interface data for the Marcellus sample where columns represent the mineralogy of fracture surface image A, and rows represent the mineralogy of the adjacent image B. Non-zero values are shaded for convenience.

	Quartz	Calcite	Dolomite	Pyrite	Kaolinite	Carbon	Other	B (total)
Quartz	0.010	0.653	0	0	0.001	0	0.017	0.680
Calcite	0.707	94.169	0.007	0.098	0.211	0.561	1.384	97.136
Kaolinite	0.003	0.210	0	0	0	0	0	0.213
Carbon	0.009	0.537	0	0	0.005	0	0.007	0.557
Other	0.006	1.401	0	0	0.003	0	0.006	1.415
A (total)	0.733	96.969	0.007	0.098	0.219	0.561	1.414	

2.4.4 Implications

By quantifying and comparing the mineralogy of the fracture surface, surrounding matrix, and bulk sample for Mancos shale, we observe that the fracture surface has a significantly higher clay content than the bulk sample, suggesting that fractures may form preferentially in clay rich lithofacies. For the Marcellus shale, the mineralogical composition of the surface, matrix, and bulk sample are consistent with each other. We believe that this discrepancy between samples is a result of mineralogy and heterogeneity. The homogeneity of the Marcellus sample (97% calcite with no distinct lithofacies) provided no preferential path for the fracture to form and as such the fracture surface reflects the matrix and bulk mineralogy and is controlled only by principal stresses. In

contrast, the Mancos sample has a variety of mineral phases with at least two distinct lithofacies, one clay-rich and one comprised of a mixture of quartz, calcite, and clay. This variation in mineralogy provides options for fracture formation where, in this study, deformation occurs primarily along the weaker, clay-rich layer. This observation suggests fracture formation depends upon mineral composition where the unit highest in clay or organic matter content may be most favorable for fracturing and thus the corresponding mineral phases more prevalent on the surface.

The reactivity of phases on the fracture surface is also a critical consideration for the possible reactive evolution of the fracture. In the Mancos sample, the fracture predominantly formed in clay rich regions. However, low fracture reactivity as a result of high kaolinite content (71-80% covering 71% of the surface) cannot be assumed due to high calcite content in the QCC regions at the surface. Calcite, the most reactive phase in this system, is more abundant on the fracture surface in comparison with the bulk mineralogy of this sample where calcite comprises 8% of the bulk mineralogy and about 14% on average of the surface. This means that the fracture surface is more reactive than would be otherwise estimated using models based on the bulk mineralogy or artificially formed fractures that fail to reflect the enhancement of reactive phases on the surface.

Chapter 3

Analysis of mineralogical spatial variation through autocorrelation

3.1 Introduction

In reactive geological systems, the accessibility of minerals plays a controlling role in the evolution of porosity and permeability (i.e. Beckingham et al. 2017, Qin and Beckingham 2020, Beckingham 2017). This may also be true in fractures, where mineral disparities can significantly impact fracture sealing capabilities (Deng, et al. 2015; Spokas, et al. 2018; Jones and Detwiler, 2016). In porous media experiments it has been found that the mineralogy of the bulk sample does not accurately represent the mineralogy accessible to the formation fluid (Landrot et al. 2012; Peters 2009; Beckingham et al. 2017; Qin and Beckingham 2019). This can be due to disconnected pores or clay coatings on grains, or in the case of fractures, the influence of weak minerals on deformation.

Researchers have explored a variety of ways to quantify mineral distribution by evaluating some degree of variation over distance. A common example of this used across both geographic and geologic applications is variograms, which work by determining the variance (γ) of a single parameter in an isotropic or anisotropic field (Gringarten & Deutsch, 2001). Based on the Kriging model in spatial statistics, variograms assume that the values of neighboring points influence each other up to some distance, or range, at which the points become independent of each other. Thus, the variogram can help us predict the mineralogy of an unknown area based on its surroundings such that within some distance *x* we can predict that the distribution of a mineral is similar to that of our known data, where beyond that distance minerals are no longer spatially correlated (i.e., the distribution is random).

Similar to the variogram, a more novel approach is the entrogram (Bianchi and Pedretti, 2017; Bianchi and Pedretti, 2018; Naimi, 2015). Based on the concept of entropy, an entrogram quantifies the degree of spatial disorder for a single parameter field measured by a relative entropy index (H_R). For entrograms, low index values (0) suggest a highly ordered system, and high values (1) suggest a more disorderly system. This information is used to estimate the amount of information needed to predict the outcome of a random process (Bianchi and Pedretti, 2018). Though Bianchi and Pedretti (2018) used entrograms to evaluate hydraulic conductivity, they provided an example of entrogram use on binary image data as well to express the broad applications of such analyses.

The final example of quantitative spatial analysis discussed here is autocorrelation. Unlike variograms and entrograms, this analysis can be performed on a multiphase sample, allowing us to compare the spatial distribution of one mineral phase with respect to another (Berryman & Blair, 1986; Blair, et al. 1996; Anovitz, et al. 2021). This can be particularly useful to yield information for reactive transport calculations by analyzing the distribution of carbonate minerals, typically very reactive phases in natural porous media samples, with respect to pores. In this analysis, a two-point autocorrelation function is used to determine the probability that both points of a random line, of random length and direction, will fall on the same mineral phase, where the results show the probability of occurrence of the phase(s) of interest. For all of these methods, it is assumed that at some point, typically large distances, the distribution becomes random.

In this study, two-point autocorrelation was used to quantitatively characterize mineral distributions at six different locations on a Mancos shale sample. The Mancos formation, located in the western United States, was used for this analysis due its heterogeneous mineral composition. The locations analyzed include four areas on a mechanically induced fracture surface, and two

areas within the nearby matrix: one parallel, and one perpendicular to the fracture surface. By performing autocorrelation analyses on a variety of areas within a single sample, we can observe not only the extent of spatial variation in a rock matrix over centimeter-scale distances, but also how mineral distributions may vary between the matrix and fracture surface with minimal impact from outside forces like formation discrepancies.

3.2 Methodology

    A two-point autocorrelation analysis was used to evaluate and compare the spatial heterogeneities of the six images using approach from Anovitz et al. (2021). The six mineral maps created from SEM images of a Mancos shale sample produced and analyzed in Chapter 2 are the focus of this analysis (Fig. 2.5 and 2.6). This approach evaluates the probability of mineral phase distribution at different correlation lengths for a given image over an increasing distance. First, a characteristic function $f(x)$ with values of only 1 and 0 must be defined. For this, ten binary images were created representing quartz, carbonate, clay, and other (encompassing all phases not previously categorized), and every pair combination of the four categories, for five of the six mineral maps. The sixth mineral map (matrix parallel to fracture) was segmented as well, with the inclusion of a pore category representing the fracture, resulting in the creation of 15 binary images. In these binaries, black represents the mineral(s) of interest, and white represents everything else (binary examples of Fig. 2.6A are given in Appendix B). Each image was also cropped to ensure an even number of pixels in both directions, and the corresponding volume fractions of each category and category pair were calculated for analysis. The correlation function for the five images without pore/fracture space is found by calculating the Fourier transform of the binary image, multiplying the result by its complex conjugate, back transforming the result, and

normalizing the final result so 0 means no correlation and 1 means perfect correlation (Anovitz, et al. 2021). For the cross-sectional matrix image, we want to analyze the distribution in two directions: along the fracture and across the fracture, into the matrix. The correlation functions used are provided below as an excerpt from Anovitz, et al. (2021):

> "Torquanto (2002) defined the characteristic function in terms of an indicator function $I^{(i)}(x)$:

$$I^{(i)}(x) = f(x) = \begin{cases} 1, x \in V_i \\ 0, x \in \bar{V}_i \end{cases} \tag{2}$$

> where V_i is the volume occupied by the ith phase, and $\bar{V}_i$ is the volume of the rest of the sample. As summarized by Anovitz et al. (2013, who used f(x) instead of $I^{(i)}x$), for a monomineralic sample, if we let f(x) = 1 for the pores, and 0 for the solid, then the first two void-void correlation functions (1- and 2-point) for an isotropic material are given by

$$\hat{S}_1 = \langle f(x) \rangle = f \tag{3}$$

$$\hat{S}_2(r) = \langle f(x)f(x+r) \rangle \tag{4}$$

> where the $\langle \ \rangle$ brackets indicate a volume average over x, r is a lag distance, $r = |r|$ for an isotropic material, and ϕ is the pore fraction.

> [...]

> correlation probabilities can also be represented using the autocovariance and/or autocorrelation coefficient functions:

$$X(r) \equiv \langle [I^{(p)}(x) - \phi_p][I^{(p)}(x+r) - \phi_p] \rangle = S_2^{(p)}(r) - \phi_p^2 , \tag{10}$$

> and

$$c(r) \equiv \frac{X(r)}{\phi_p(1-\phi_p)} = \frac{X(r)}{\phi_p\phi_g} \tag{11}$$
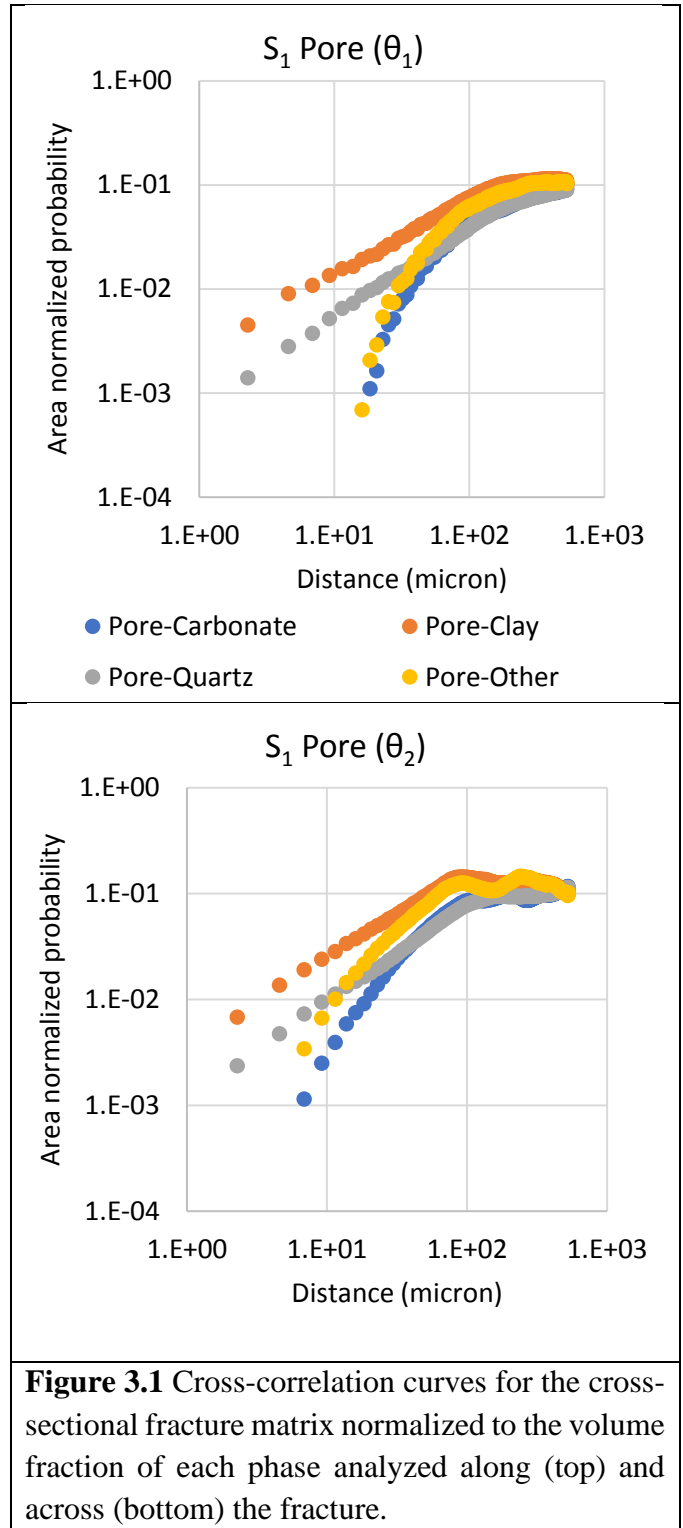
> where ϕ_g is the volume fraction of a grain phase, ϕ_p is the volume fraction of pores, and $\phi_p + \phi_g = 1$. $c(r)$ is a normalized version of $X(r)$."

3.3 Results

The rock matrix perpendicular to the fracture (Fig. 2.6A) was analyzed vertically along the fracture and horizontally into the matrix (these angles will be differentiated as θ_1 and θ_2, respectively). The resulting data is shown in Figure 3.1 where the data is normalized with respect to pores to evaluate the spatial relationship between mineral phases without the influence of their abundance. Here, the area normalized probabilities of clay, quartz, carbonate, and other as a function of distance from any point in the fracture are shown, where the initial point (S_1) is always a fracture pixel. Figure 3.1 shows that in both directions, clay is most likely to be present at any distance from a given fracture pixel. When looking into the matrix (θ_2) approximately 7 microns from the fracture, clay and quartz are 16.7 and 6.6 times more likely to be present than carbonate. When compared to the volume fractions for Fig. 2.6A in Table 2.2, clay is 1.7 times more abundant than carbonate, and quartz is 4.5 times more abundant than carbonate. As we look closer to the fracture at about 2.3 microns, clay is approximately 2.8 times more likely to be present

Figure 3.1 Cross-correlation curves for the cross-sectional fracture matrix normalized to the volume fraction of each phase analyzed along (top) and across (bottom) the fracture.

than quartz, and the discrepancies between these phases and carbonate increase further. Therefore, clay and quartz are significantly more likely to be present near the fracture surface than carbonate minerals. Additional information that can be read from Figure 3.1 is that for θ_2, the clay distribution becomes random at around 200 microns from any point in the fracture. This observation further describes the presence of a clay rich layer surrounding the fracture, estimating it to be roughly 400 microns thick.

The cross-sectional fracture matrix is also analyzed with respect to carbonate, quartz, and clay in both directions. Because each of these graphs are extremely similar in both directions, we will only discuss the data for θ_2 here. However, graphs for θ_1 can be found in Appendix B. Figure 3.2, 3.3, and 3.4 show the θ_2 graphs for each mineral phase as a function of distance from any carbonate, quartz, or clay pixel, respectively. In the autocorrelation curves for distance from carbonate minerals (Fig. 3.2), the values at short distances (less than 10 microns) are relatively proportional for quartz and clay, with other phases only slightly more present. The changes increase at distances greater than 10 microns. The probability of quartz pixels to be present at distances 10 microns and larger from calcite is highest, followed by clay, then other. The significant bend in the carbonate-carbonate curve (blue) denotes the average grain size of the carbonate minerals (approximately 57 microns). It should be noted that this size is based on both calcite and dolomite grains. Similarly, the autocorrelation curves for clay minerals encompasses both kaolinite and illite. In this graph (Fig. 3.4), quartz is about 1.9 times more likely than carbonate to occur next to clay minerals. This is also reflected in the curves for quartz (Fig. 3.3) in the quartz-clay curve that shows clay is more likely than other phases to be found close to quartz

pixels, reflecting that clay coatings are more likely to occur on quartz grains than carbonate minerals.
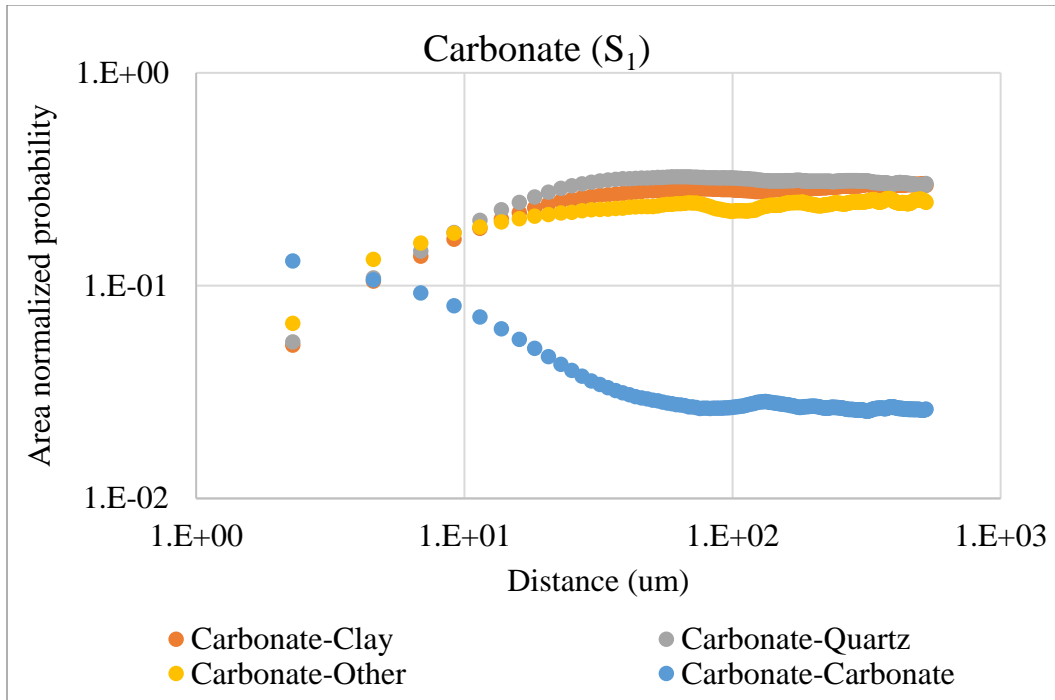

Figure 3.2. Autocorrelation/cross-correlation for the cross-sectional fracture matrix (Fig. 2.6B) at θ_2 normalized to the volume fraction of each phase with respect to carbonate.
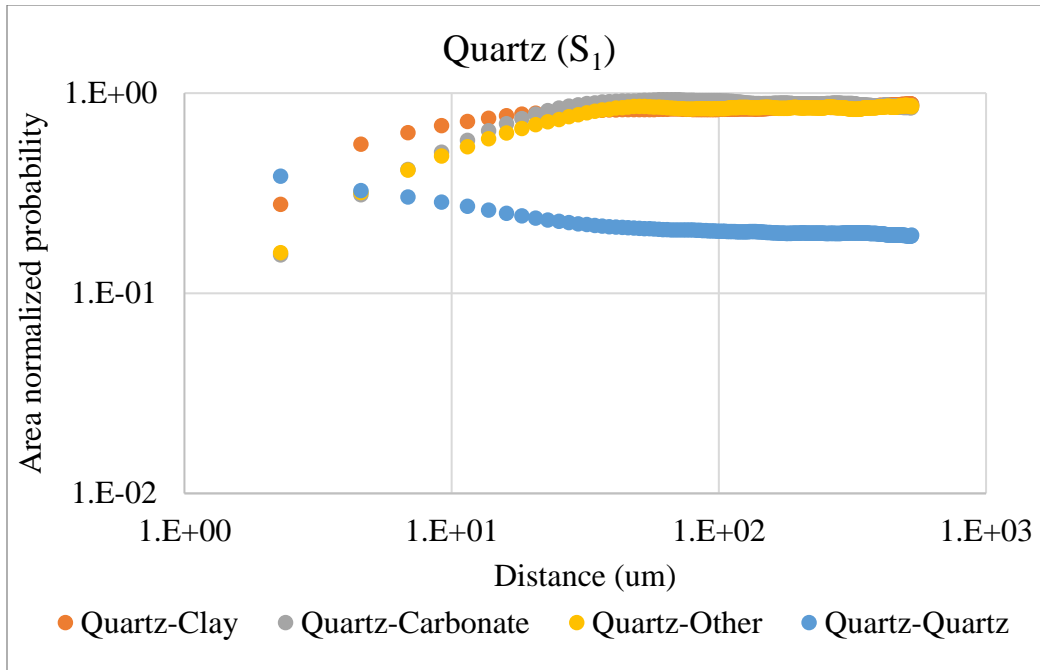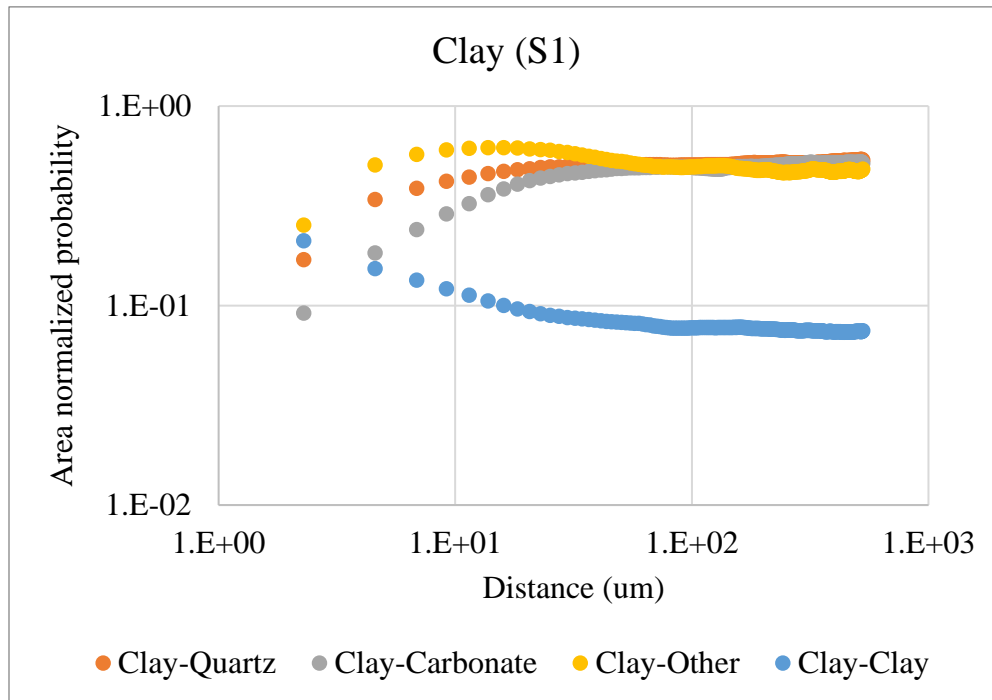
Figure 3.3. Autocorrelation/cross-correlation for the cross-sectional fracture matrix (Fig. 2.6B) at θ_2 normalized to the volume fraction of each phase with respect to quartz.

Figure 3.4. Autocorrelation/cross-correlation for the cross-sectional fracture matrix (Fig. 2.6B) at θ_2 normalized to the volume fraction of each phase with respect to clay.

In Figures 3.1 through 3.4 we analyze the matrix mineral distribution just beyond the fracture surface in two directions. However, to compare a more general matrix distribution with that at the fracture surface, the autocorrelation/cross-correlation analysis is carried out on Figures 2.5 and 2.6B radially. Figures 3.5, 3.6 and 3.7 show the resulting autocorrelation of the matrix parallel to the fracture evaluated that reflects distance from carbonate, quartz, and clay pixels.
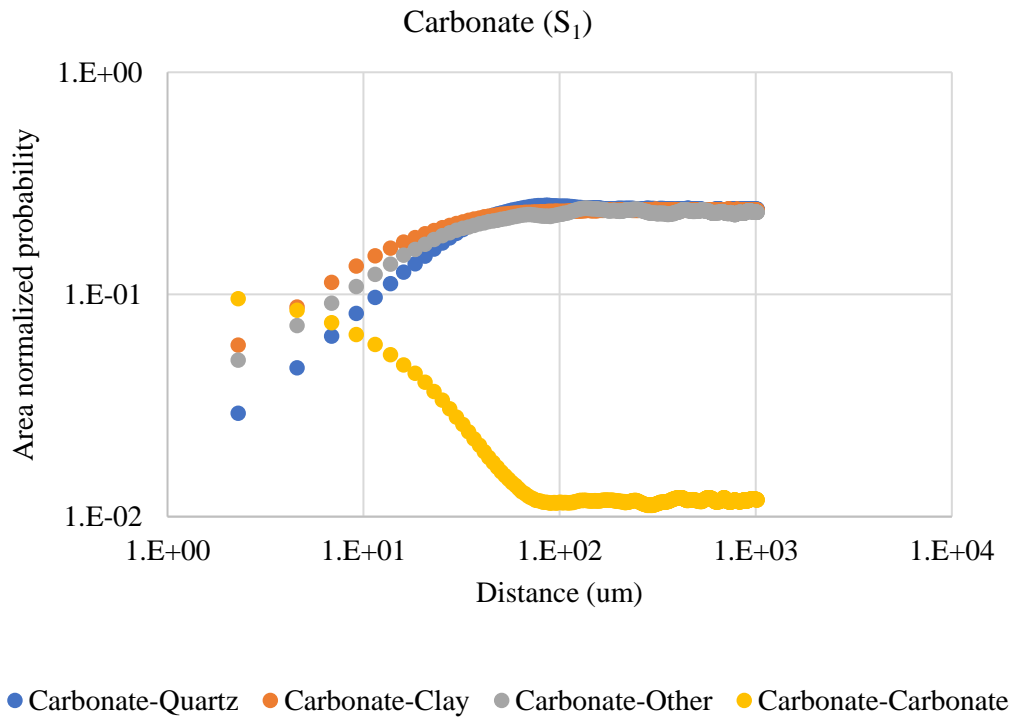
Figure 3.5. Autocorrelation/cross-correlation for the parallel to fracture matrix (Fig. 2.6B) normalized to the volume fraction of each phase with respect to carbonate
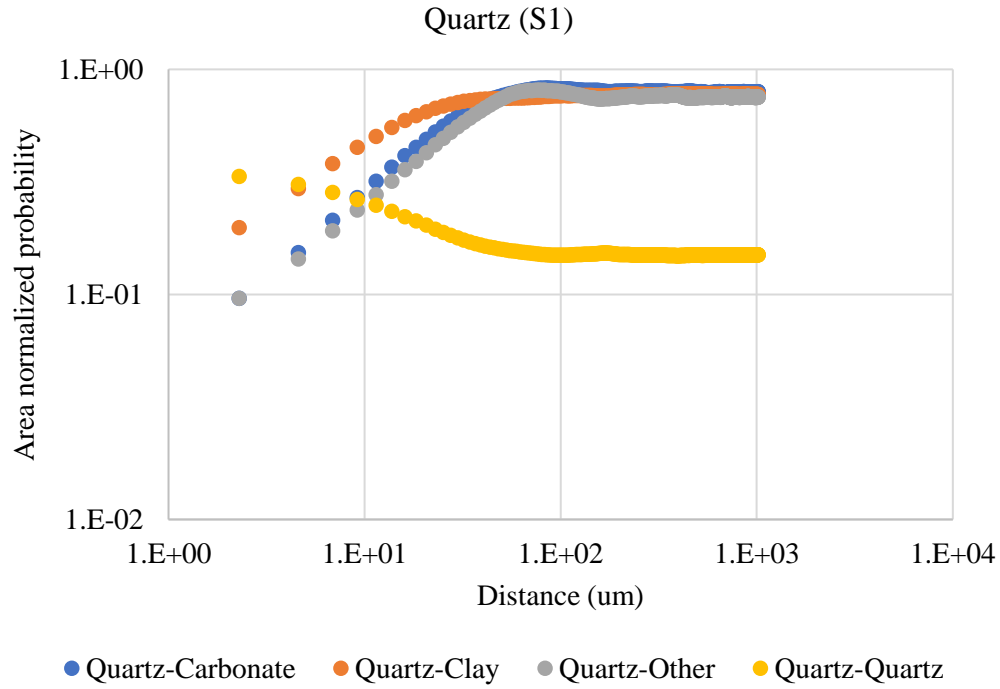
Figure 3.6. Autocorrelation/cross-correlation for the parallel to fracture matrix (Fig. 2.6B) normalized to the volume fraction of each phase with respect to quartz.
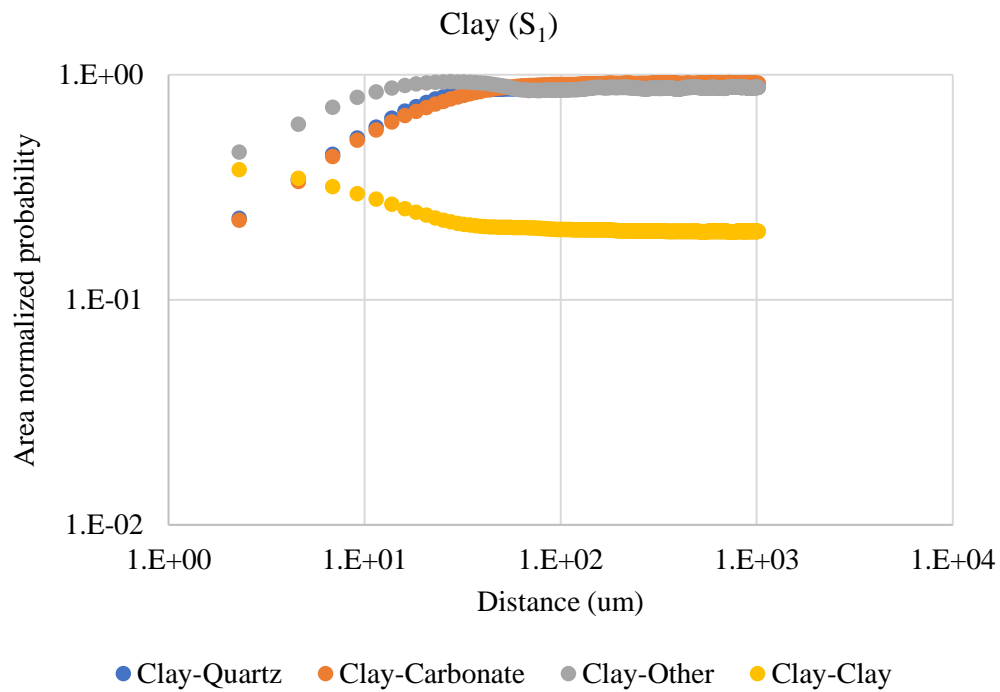
Figure 3.7. Autocorrelation/cross-correlation for the parallel to fracture matrix (Fig. 2.6B) normalized to the volume fraction of each phase with respect to clay.

Figures 3.8 through 3.19 show these results for fracture surface areas A, B, C, and D as shown and described in Figure 2.5. From the carbonate graphs (Figures 3.5, 3.8, 3.11, 3.14, and 3.17) we observe that the average grain size in the matrix is larger and more uniform than that on the fracture surface, suggesting the surface has a wider distribution of carbonate grain sizes. A steeper slope for all phases is observed in all graphs in the matrix compared with the fracture surface (Figures 3.5 through 3.19). This distinct difference in slope suggests that minerals at the fracture surface are more uniformly distributed than those in the matrix.

When comparing the QCC and clay-rich lithofacies at the fracture surface we notice that quartz and carbonate are more uniformly distributed in the clay-rich facies described by a flatter curve in these regions (Figures 3.8, 3.9, 3.11, 3.12, 3.14, 3.15, 3.17, and 3.18). A final observation can be made for the carbonate and quartz graphs comparing the matrix and surface where, for both graphs in the matrix, all cross-correlation curves converge and become random. In contrast to this, one QCC area (Fig. 2.5A, Fig. 3.8-3.10) and both clay-rich areas (Fig. 2.5C and 2.5D, Fig. 3.14, 3.15, 3.17, and 3.18) do not completely converge at large distances. These observations of the fracture surface and matrix suggest a more uniform distribution of carbonate and quartz minerals at the fracture surface, with a wider variety of grain sizes than what is found in the matrix.

It is also found that at some distance in the matrix the distribution will always become random, where distribution is a function of mineral abundance. However, at the fracture surface this is not necessarily the case. For the QCC area (Fig. 2.5A, Fig. 3.8-3.10), the nonconverging curve is related to the other group where we can assume this is due to the variety of minerals involved. An outlier, however, is clay-rich area Fig. 2.5D (Fig. 3.17). where carbonate is most correlated to quartz, but quartz is more correlated to clay and other. It is unlikely such large disparities are an artifact of the autocorrelation function as they do not exist in the other figures.

As such we may consider that either the spatial distribution of Fig. 2.5D is an outlier, or that the

distribution here is not inherently random and is in fact controlled by fracture formation.
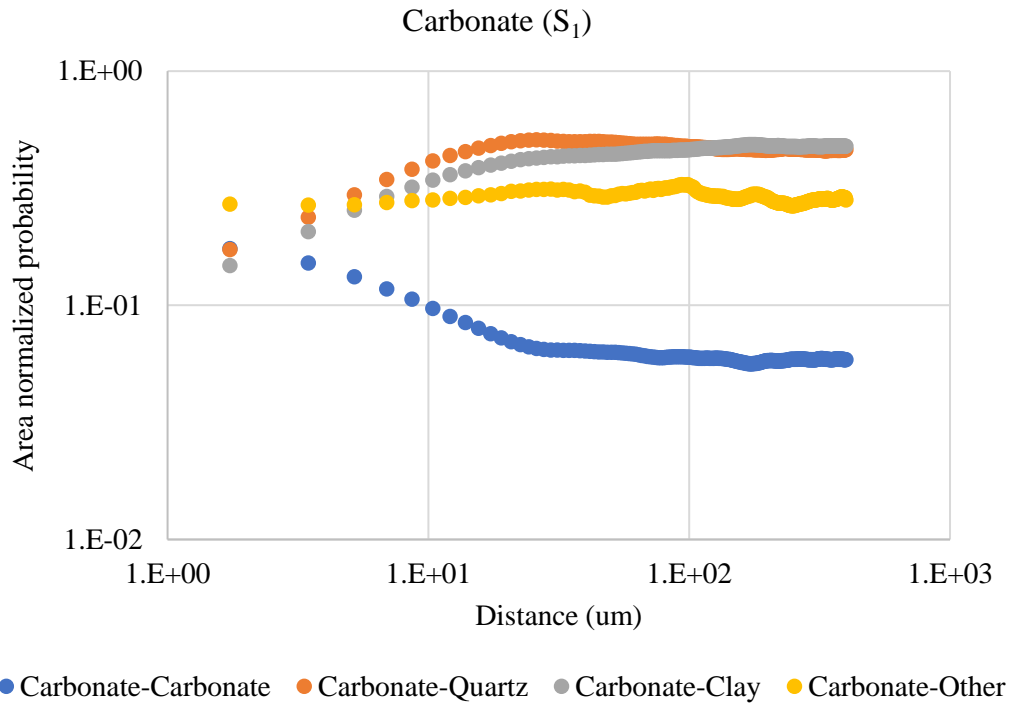

Figure 3.8. Autocorrelation/cross-correlation for the QCC fracture surface A (Fig. 2.5A) normalized to the volume fraction of each phase with respect to carbonate.
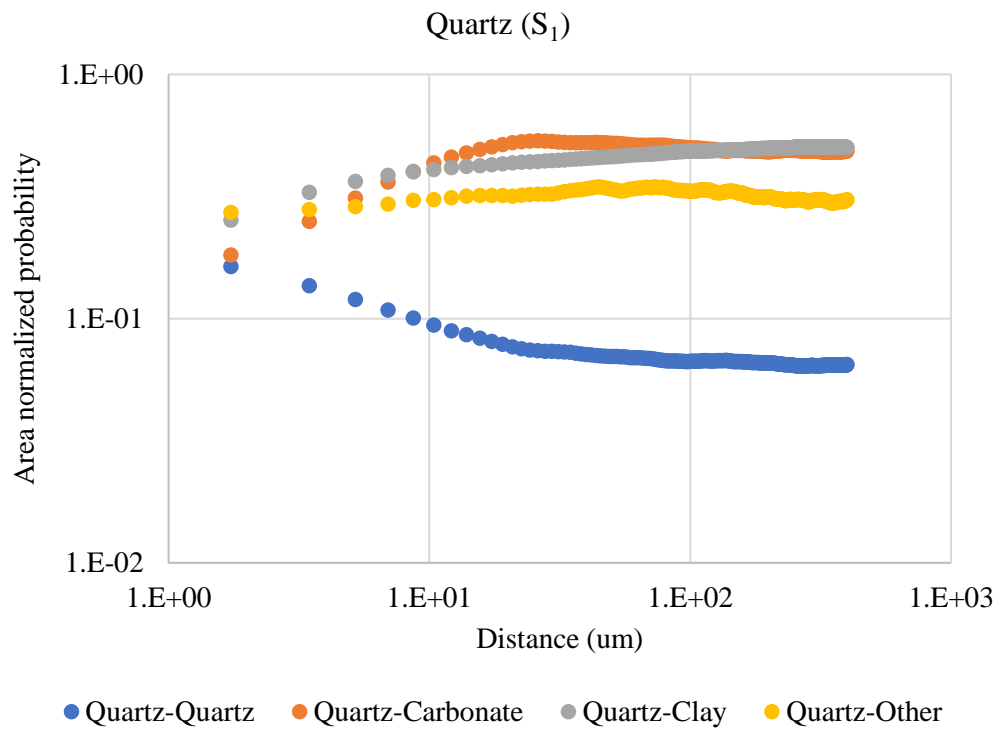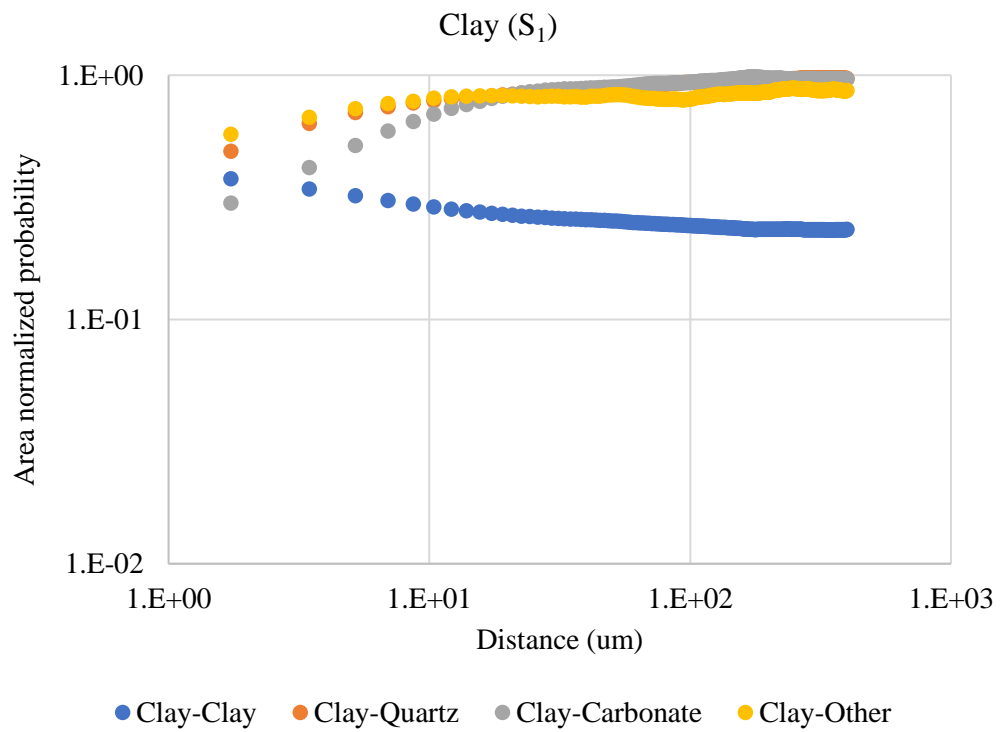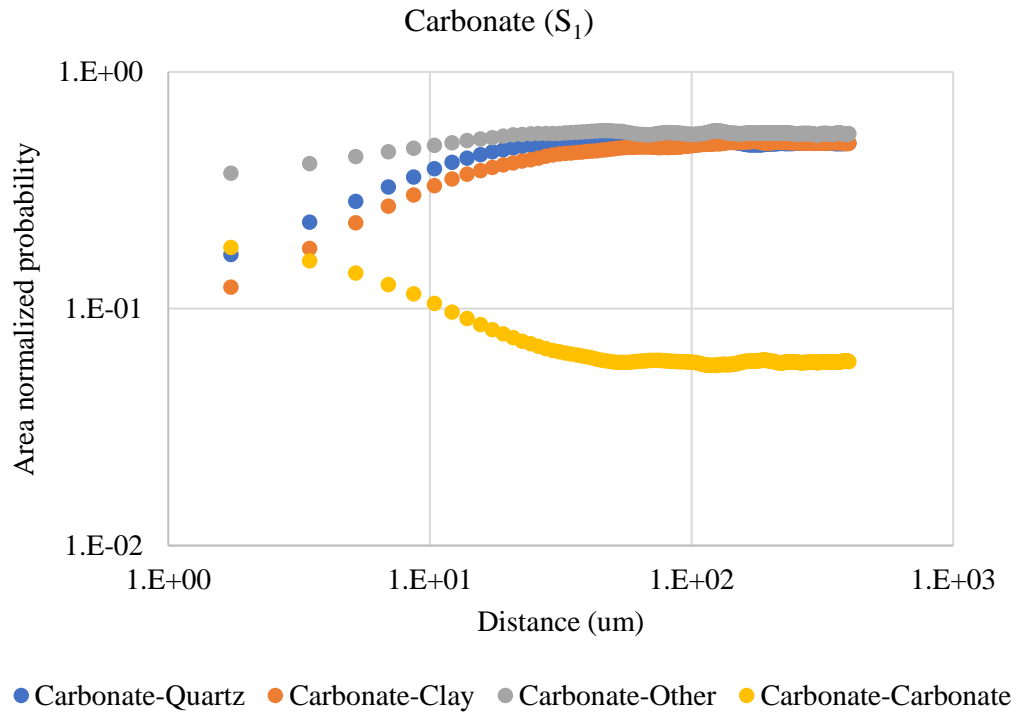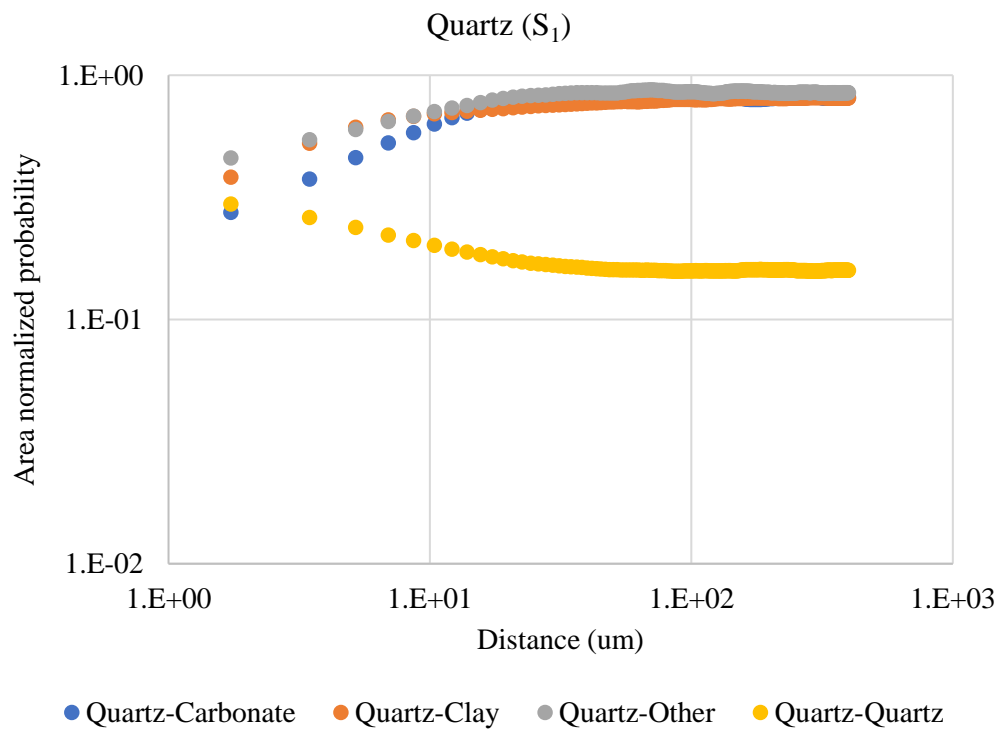
Figure 3.9. Autocorrelation/cross-correlation for the QCC fracture surface A (Fig. 2.5A) normalized to the volume fraction of each phase with respect to quartz.
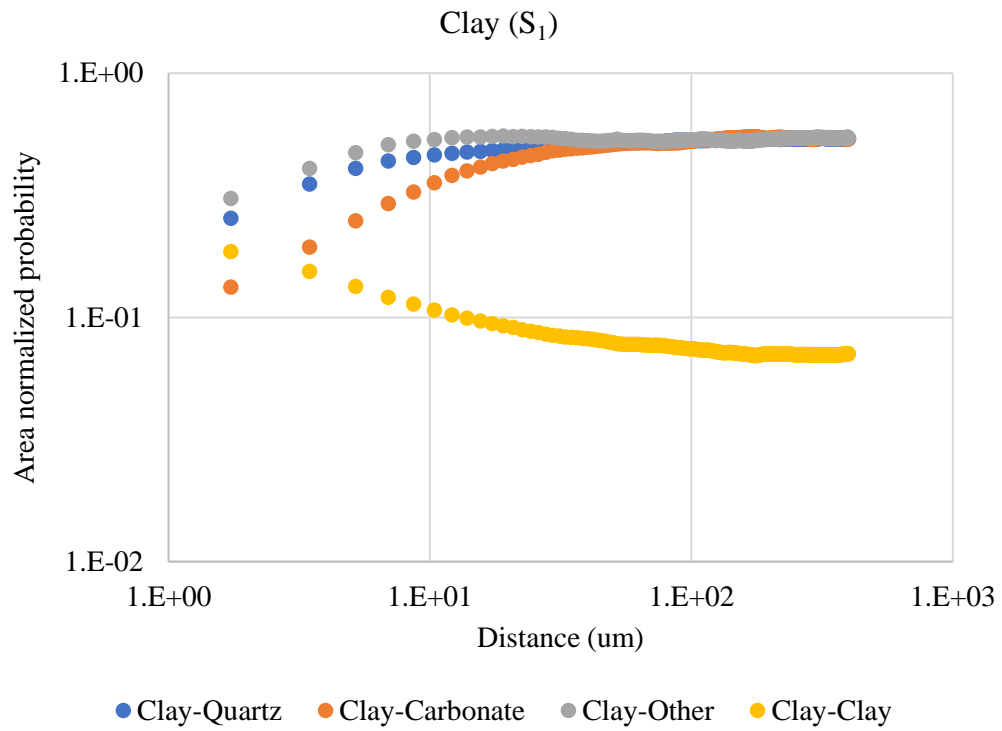
Figure 3.10. Autocorrelation/cross-correlation for the QCC fracture surface A (Fig. 2.5A) normalized to the volume fraction of each phase with respect to clay.

Figure 3.11. Autocorrelation/cross-correlation for the QCC fracture surface B (Fig. 2.5B) normalized to the volume fraction of each phase with respect to carbonate.
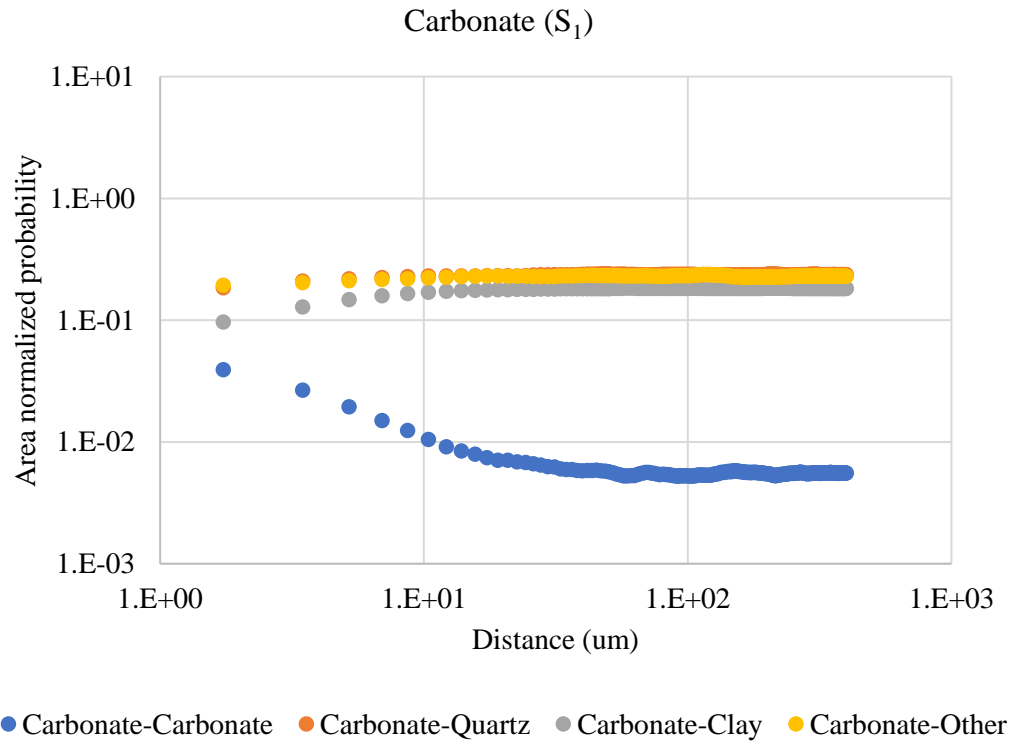
Figure 3.12. Autocorrelation/cross-correlation for the QCC fracture surface B (Fig. 2.5B) normalized to the volume fraction of each phase with respect to quartz.

Figure 3.13. Autocorrelation/cross-correlation for the QCC fracture surface B (Fig. 2.5B) normalized to the volume fraction of each phase with respect to clay.

Figure 3.14. Autocorrelation/cross-correlation for the clay-rich fracture surface C (Fig. 2.5C) normalized to the volume fraction of each phase with respect to carbonate.
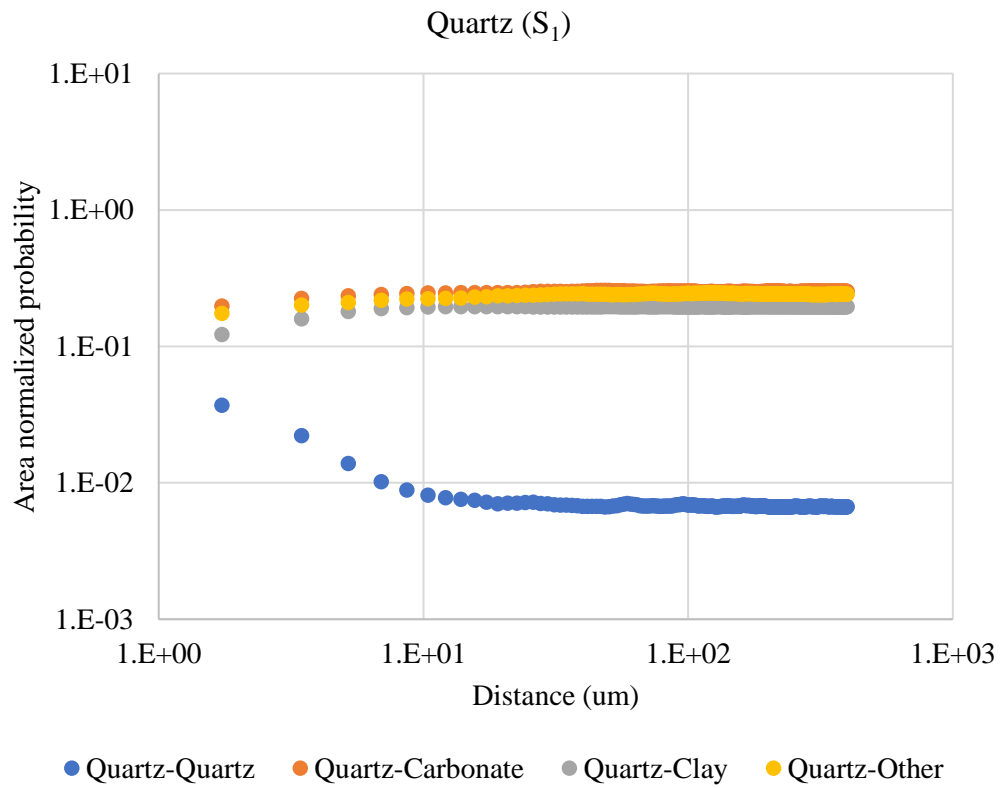
Figure 3.15. Autocorrelation/cross-correlation for the clay-rich fracture surface C (Fig. 2.5C) normalized to the volume fraction of each phase with respect to quartz.
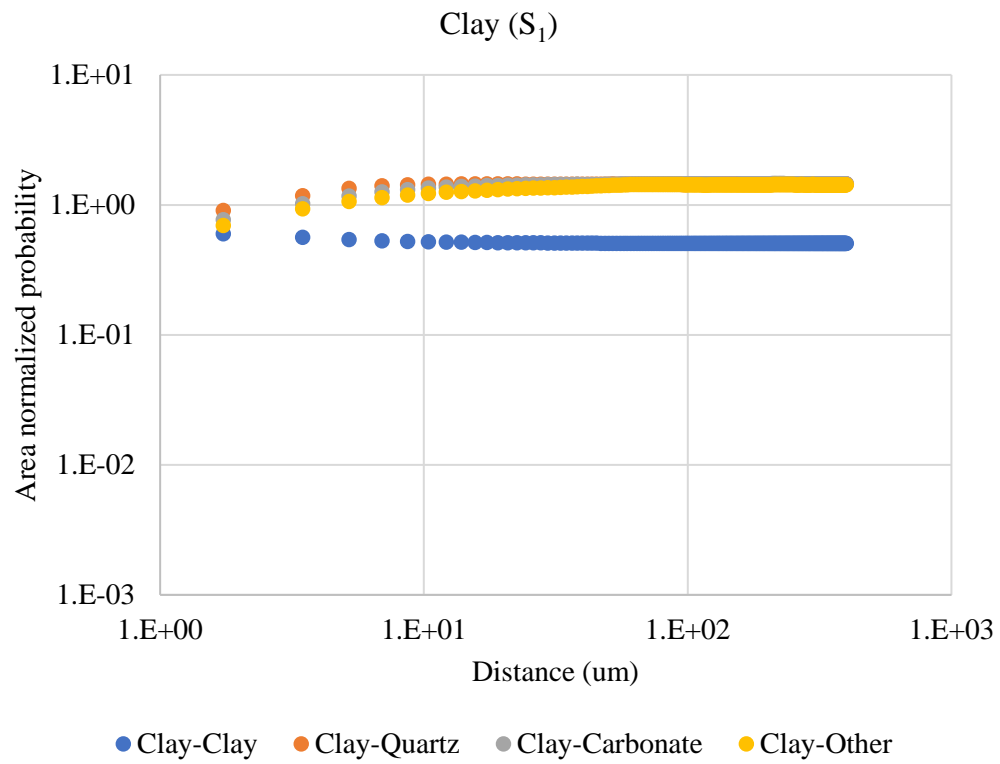
Figure 3.16. Autocorrelation/cross-correlation for the clay-rich fracture surface C (Fig. 2.5C) normalized to the volume fraction of each phase with respect to clay.
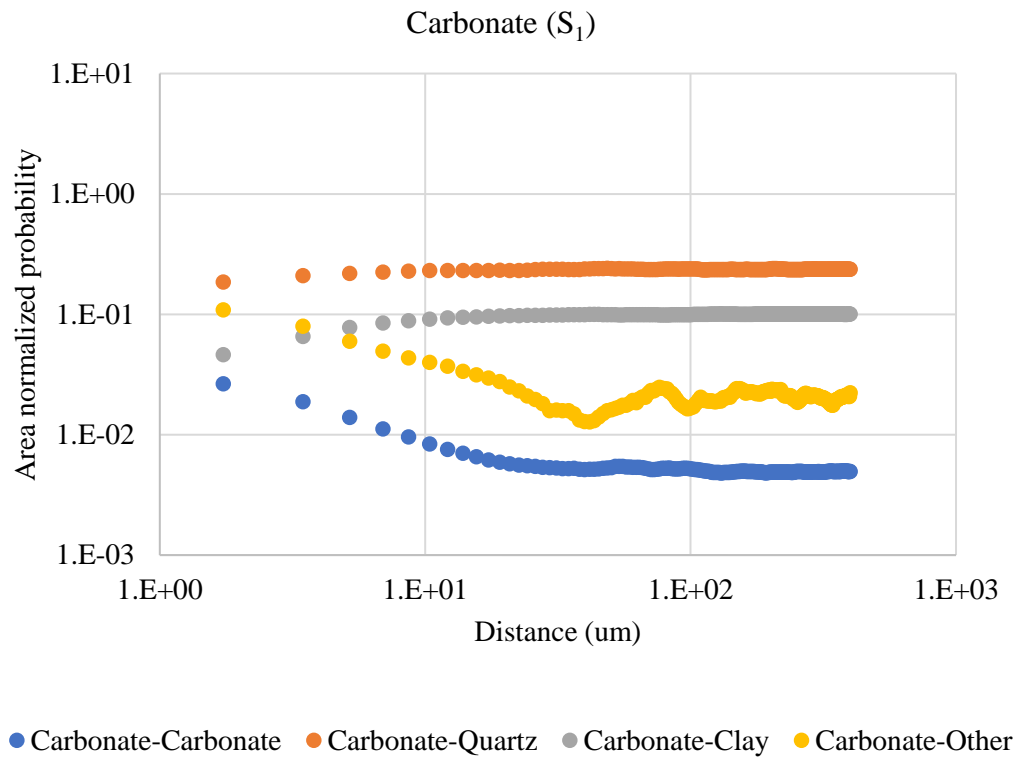
Figure 3.17. Autocorrelation/cross-correlation for the clay-rich fracture surface D (Fig. 2.5D) normalized to the volume fraction of each phase with respect to carbonate.
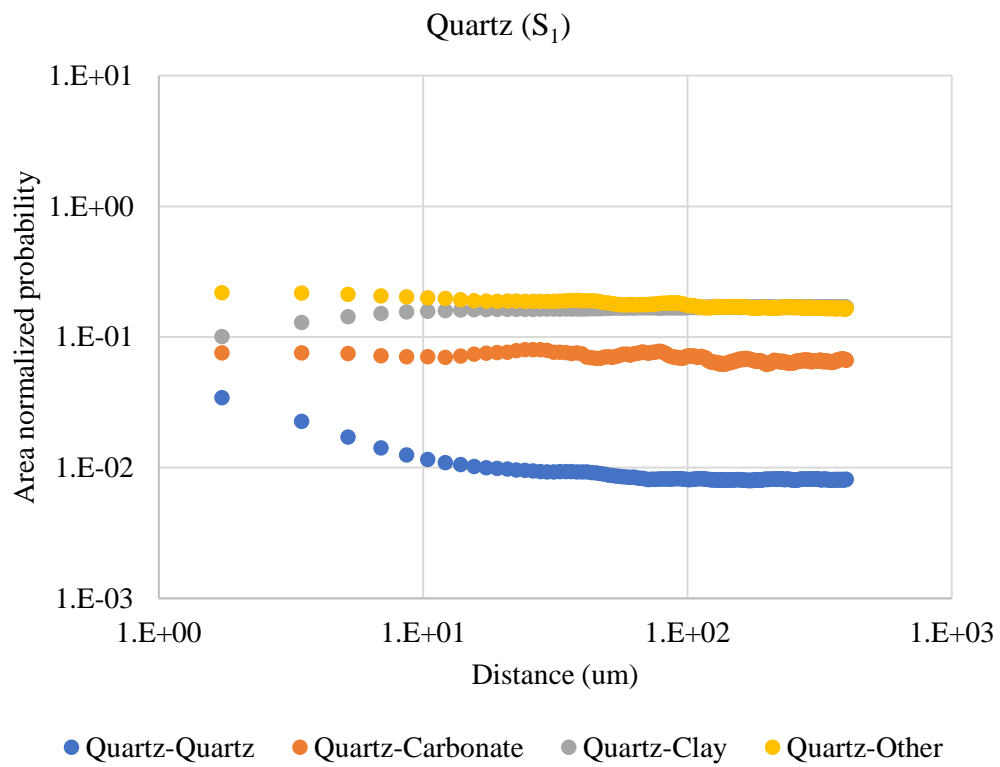
Figure 3.18. Autocorrelation/cross-correlation for the clay-rich fracture surface D (Fig. 2.5D) normalized to the volume fraction of each phase with respect to quartz.
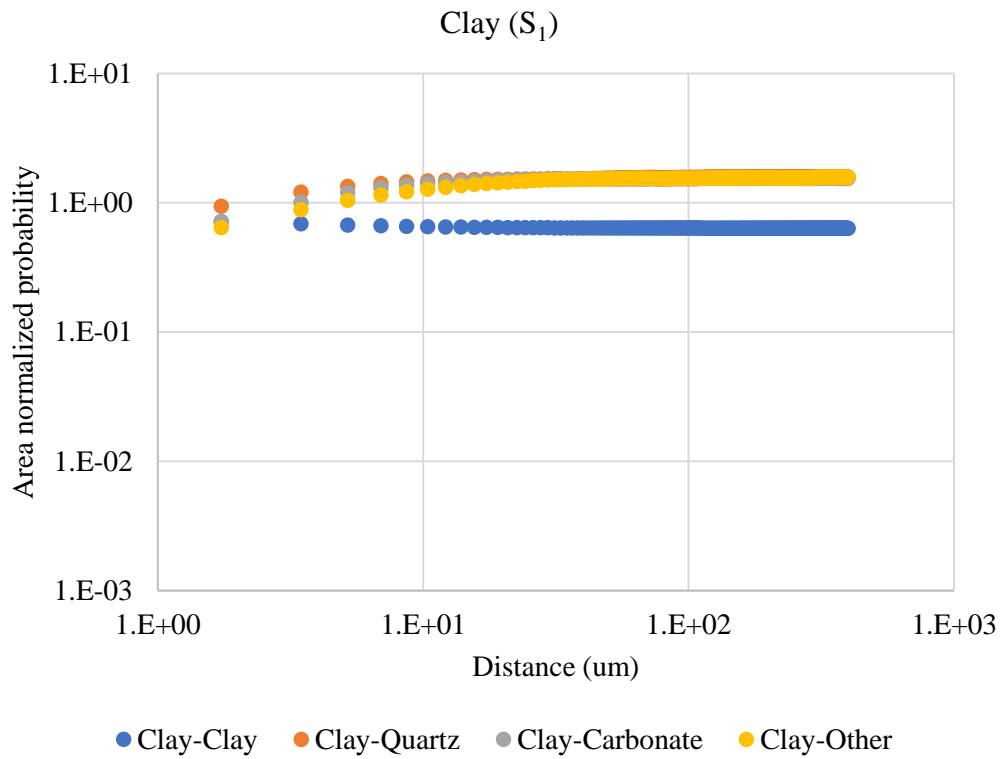
Figure 3.19. Autocorrelation/cross-correlation for the clay-rich fracture surface D (Fig. 2.5D) normalized to the volume fraction of each phase with respect to clay.

3.4 Conclusions

From Chapter 2 we established that fracture surface mineralogy is significantly higher in clay than would be expected from XRD data suggesting fracture formation is partial to clay-rich lithofacies. However, this conclusion was drawn strictly through the quantification of mineral abundance. Here, we expand on this abundance data by quantifying mineral distributions at the fracture surface and beyond. We observe that the clay-rich lithofacies through which the fracture form, extend up to roughly 200 microns into the matrix beyond the fracture walls. Within this facies, clay minerals are 16.7 times more likely than carbonate minerals to appear 7 microns from the fracture, despite clay being only 1.7 times more abundant than carbonate in the XRD data. This probability further increases as distance from the fracture decreases. When we compare the fracture surface distribution to that of the matrix it is clear that the surface has a more uniform mineral distribution at any distance, with a wider variety of carbonate grain sizes. When evaluated with respect to any phase, the matrix distribution will always become random at large distances. However, this is not necessarily true for the fracture surface, where some phases have higher degrees of correlation than others even at large distances, particularly surface area D (Fig. 2.5D). To determine if this is true for all fractures, more samples would need to be examined.

Chapter 4

Conclusions and contributions to new knowledge

In this study, Mancos and Marcellus shale samples were subject to unconfined compression until an initial fracture formed. The samples with fracture surfaces most suitable for imaging were chosen as subjects for SEM-EDS analysis where representative mineral maps were created for both the surface and near fracture matrix. This work then takes an in depth look at fracture surface mineralogy in homogenous and heterogenous shale samples to infer the influence of mineralogy on fracture formation. This type of analysis has not been previously done in the literature and this work is the first to quantify and compare the mineralogy of an unaltered fracture surface with that of the matrix and bulk sample.

For the heterogeneous Mancos shale sample, the fracture surface mineralogy proved to be significantly different from that of the bulk, containing 3.5 times more clay on average. The surface also contained 1.4 times more clay on average when compared to the longitudinal matrix, and 2.4 times more when compared to the cross-sectional matrix. For the Mancos shale, classified as brittle by Holt et al. (2015), it is clear that weak clay minerals are more abundant on the fracture surface than anywhere else in sample. Furthermore, cross-correlation results of the cross-sectional matrix show that clay minerals have the highest probability of occurring near the fracture when compared with quartz and carbonate minerals. Accompanied with the findings of Yoon, et al. 2019, we believe it is very likely that weak minerals, such as clay, will be more prevalent on the fracture surface than would be expected from bulk data.

In regard to the Marcellus shale sample, mineralogy at the fracture surface was consistent with that of the bulk and surrounding matrices. Though clay exists in this sample, it was observed

in SEM only within pre-existing deformations, suggesting it precipitated after the fact. Due to the homogeneity of this sample, we cannot determine any relationship between mineralogy and fracture formation.

The autocorrelation data for the Mancos shale allowed us to quantify the mineral distributions and expand on our results beyond simply mineral abundance. In the matrix just behind the fracture walls it was found that clay is 16.7 times more likely than carbonate to be present within 7 microns of the fracture. The results from this image further defined the clay-rich lithofacies chosen by the fracture, estimating that it extends up to roughly 200 microns into the matrix beyond the fracture. When comparing the matrix and fracture surfaces it was found that the surface has a more uniform distribution of minerals and a wider range of grain sizes. Perhaps the most noticeable difference between the surface and matrix is that the spatial distribution in the matrix always became random and the surface did not (Fig. 2.5D, Fig. 3.7 most notably). Due to the small sample size of two images for this particular area, we cannot determine if this data is an outlier or a true result of fracture surface mineralogy. Though spatial analyses are common in porous media applications, the quantification of mineral distribution changes with respect to fractures is done for the first time in this work.

The implications on what these results mean for fracture evolution in a CCS system will be dependent upon the heterogeneity of the formation. In a highly heterogeneous formation like Mancos shale, fracture evolution will depend heavily upon the reactivity of the expected clay phase. In Figure 2.5, clay was defined at the fracture surface exclusively as kaolinite. However, in the matrix and XRD, illite is the most abundant clay phase. Because of their distinct chemical differences, it is unlikely that the fracture surface has high illite content, though it is also unlikely that there will be none. Though this will of course impact fracture reactivity, the most reactive

phase in this sample is calcite. Overall, the fracture surface contains 13.8% calcite, 15.9% quartz, and 64.4% clay based on the average mineralogies of each lithofacies and their abundance on the surface. When presented this way, calcite content at the surface is relatively consistent with that of the matrix and XRD, though clay is still significantly higher. However, carbonate minerals are not evenly distributed across the fracture surface and are instead concentrated in high calcite zones (QCC layer). As a result, it is likely that surface dissolution will occur primarily at QCC regions (29% of the surface) causing aperture increases at small, focused areas and flow paths perpendicular to the fracture. From autocorrelation, we see that approximately 7 microns of mineral dissolution is required for additional carbonate minerals to be exposed in abundance. With dissolution focused at QCC regions, potential for fluid to access this additional calcite increases. As a result, we can hypothesize that fracture evolution can increase caprock permeability in more directions than simply through the fracture.

References

1. Hansen, J. E., Sato, M., Lacis, A., Ruedy, R., Tegen, I., & Matthews, E. (1998). Climate forcings in the Industrial era. In *Proceedings of the National Academy of Sciences of the United States of America* (Vol. 95, Issue 22). https://doi.org/10.1073/pnas.95.22.12753
2. IPCC. (2007). IPCC Fourth Assessment Report: Climate Change 2007 (AR4) - Synthesis Report. In *Intergovernmental Panel on Climate Change [Core Writing Team IPCC]*.
3. IPPC. (2014). IPCC, 2014: Climate Change 2014: Mitigation of Climate Change. Contribution of Working Group III to the Fifth Assessment Report of the Intergovernmental Panel on Climate Change. In *Cambridge University Press*.
4. Gillet-Chaulet, F., Gagliardini, O., Seddik, H., Nodet, M., Durand, G., Ritz, C., Zwinger, T., Greve, R., & Vaughan, D. G. (2012). Greenland ice sheet contribution to sea-level rise from a new-generation ice-sheet model. *Cryosphere*, *6*(6). https://doi.org/10.5194/tc-6-1561-2012
5. Goelzer, H., Nowicki, S., Payne, A., Larour, E., Seroussi, H., Lipscomb, W. H., Gregory, J., Abe-Ouchi, A., Shepherd, A., Simon, E., Agosta, C., Alexander, P., Aschwanden, A., Barthel, A., Calov, R., Chambers, C., Choi, Y., Cuzzone, J., Dumas, C., … Van Den Broeke, M. (2020). The future sea-level contribution of the Greenland ice sheet: A multi-model ensemble study of ISMIP6. *Cryosphere*, *14*(9). https://doi.org/10.5194/tc-14-3071-2020
6. Biermann, F., & Boas, I. (2008). Protecting Climate Refugees: The Case for a Global Protocol. *Environment*, *50*(6). https://doi.org/10.3200/ENVT.50.6.8-17
7. Myers, N. (2002). Environmental refugees: A growing phenomenon of the 21st century. *Philosophical Transactions of the Royal Society B: Biological Sciences*, *357*(1420). https://doi.org/10.1098/rstb.2001.0953
8. Yu, K. M. K., Curcic, I., Gabriel, J., & Tsang, S. C. E. (2008). Recent advances in CO2 capture and utilization. In *ChemSusChem* (Vol. 1, Issue 11). https://doi.org/10.1002/cssc.200800169
9. Oelkers, E. H., Gislason, S. R., & Matter, J. (2008). Mineral carbonation of CO2. *Elements*, *4*(5). https://doi.org/10.2113/gselements.4.5.333
10. Miocic, J. M., Gilfillan, S. M. V., Roberts, J. J., Edlmann, K., McDermott, C. I., & Haszeldine, R. S. (2016). Controls on CO2 storage security in natural reservoirs and implications for CO2 storage site selection. *International Journal of Greenhouse Gas Control*, *51*. https://doi.org/10.1016/j.ijggc.2016.05.019
11. Watson, M. N., & Gibson-Poole, C. M. (2005). Reservoir selection for optimised geological injection and storage of carbon dioxide: A combined geochemical and stratigraphic perspective. *4th Annual Conference on Carbon Capture and Sequestration*.
12. Ellis, B., Peters, C., Fitts, J., Bromhal, G., McIntyre, D., Warzinski, R., & Rosenbaum, E. (2011). Deterioration of a fractured carbonate caprock exposed to CO 2-acidified brine flow. *Greenhouse Gases: Science and Technology*. https://doi.org/10.1002/ghg.25
13. Major, J. R., Eichhubl, P., Dewers, T. A., & Olson, J. E. (2018). Effect of CO2–brine–rock interaction on fracture mechanical properties of CO2 reservoirs and seals. *Earth and Planetary Science Letters*. https://doi.org/10.1016/j.epsl.2018.07.013

14. Fitts, J. P., Ellis, B. R., Deng, H., & Peters, C. A. (2012). Geochemical controls on fracture evolution in carbon sequestration. *46th US Rock Mechanics / Geomechanics Symposium 2012*, *3*.

15. Tian, H., Xu, T., Zhu, H., Yang, C., & Ding, F. (2019). Heterogeneity in mineral composition and its impact on the sealing capacity of caprock for a CO 2 geological storage site. *Computers and Geosciences*. https://doi.org/10.1016/j.cageo.2019.01.015

16. Fitts, J. P., & Peters, C. A. (2013). Caprock fracture dissolution and CO2 leakage. *Reviews in Mineralogy and Geochemistry*. https://doi.org/10.2138/rmg.2013.77.13

17. Bensinger, J., & Beckingham, L. E. (2020). CO2 storage in the Paluxy formation at the Kemper County CO2 storage complex: Pore network properties and simulated reactive permeability evolution. *International Journal of Greenhouse Gas Control*, *93*. https://doi.org/10.1016/j.ijggc.2019.102887

18. Beckingham, L., Bensinger, J., Steinwinder, J., & Sabo, M. (2020). *Porosity-Permeability Evolution in Heterogeneous Mineral Dissolution and Precipitation Scenarios*. https://doi.org/10.46427/gold2020.154

19. Deng, H., Fitts, J. P., Crandall, D., McIntyre, D., & Peters, C. A. (2015). Alterations of Fractures in Carbonate Rocks by CO2-Acidified Brines. *Environmental Science and Technology*. https://doi.org/10.1021/acs.est.5b01980

20. Spokas, K., Peters, C. A., & Pyrak-Nolte, L. (2018). Influence of Rock Mineralogy on Reactive Fracture Evolution in Carbonate-Rich Caprocks. *Environmental Science and Technology*. https://doi.org/10.1021/acs.est.8b01021

21. Jones, T. A., & Detwiler, R. L. (2016). Fracture sealing by mineral precipitation: The role of small-scale mineral heterogeneity. *Geophysical Research Letters*. https://doi.org/10.1002/2016GL069598

22. Gutierrez, M., Øino, L. E., & Nygård, R. (2000). Stress-dependent permeability of a de-mineralised fracture in shale. *Marine and Petroleum Geology*. https://doi.org/10.1016/S0264-8172(00)00027-1

23. Guo, L., Jiang, Z. xing, & Guo, F. (2015). Mineralogy and fracture development characteristics of marine shale-gas reservoirs: A case study of Lower Silurian strata in southeastern margin of Sichuan Basin, China. *Journal of Central South University*. https://doi.org/10.1007/s11771-015-2704-6

24. Tian, X., & Daigle, H. (2019). Preferential mineral-microfracture association in intact and deformed shales detected by machine learning object detection. *Journal of Natural Gas Science and Engineering*. https://doi.org/10.1016/j.jngse.2019.01.003

25. Ding, W., Li, C., Li, C., Xu, C., Jiu, K., Zeng, W., & Wu, L. (2012). Fracture development in shale and its relationship to gas accumulation. *Geoscience Frontiers*. https://doi.org/10.1016/j.gsf.2011.10.001

26. Yoon, H., Ingraham, M. D., Grigg, J., Rosandick, B., Mozley, P., Rinehart, A., Mook, W. M., & Dewers, T. (2019). Impact of Depositional and Diagenetic Heterogeneity on Multiscale Mechanical Behavior of Mancos Shale, New Mexico and Utah, USA. In *Memoir 120: Mudstone Diagenesis: Research Perspectives for Shale Hydrocarbon Reservoirs, Seals, and Source Rocks*. https://doi.org/10.1306/13672214m1213824

27. Gale, J. F. W., Laubach, S. E., Olson, J. E., Eichhubl, P., & Fall, A. (2017). Natural fractures in shale: A review and new observations. *AAPG Bulletin*. https://doi.org/10.1306/08121413151

28. Na, S. H., Sun, W. C., Ingraham, M. D., & Yoon, H. (2017). Effects of spatial heterogeneity and material anisotropy on the fracture pattern and macroscopic effective toughness of Mancos Shale in Brazilian tests. *Journal of Geophysical Research: Solid Earth*. https://doi.org/10.1002/2016JB013374

29. Brunhoeber, O. M., Arakkal, D., Ji, R., Miletić, M., & Beckingham, L. E. (2020). Impact of mineral composition and distribution on the mechanical properties of porous media. *E3S Web of Conferences*, *205*. https://doi.org/10.1051/e3sconf/202020502006

30. Laubach, S. E., Olson, J. E., & Cross, M. R. (2009). Mechanical and fracture stratigraphy. *AAPG Bulletin*, *93*(11). https://doi.org/10.1306/07270909094

31. Holt, R. M., Fjær, E., Stenebråten, J. F., & Nes, O. M. (2015). Brittleness of shales: Relevance to borehole collapse and hydraulic fracturing. *Journal of Petroleum Science and Engineering*. https://doi.org/10.1016/j.petrol.2015.04.006

32. Zhang, D., Ranjith, P. G., & Perera, M. S. A. (2016). The brittleness indices used in rock mechanics and their application in shale hydraulic fracturing: A review. *Journal of Petroleum Science and Engineering*. https://doi.org/10.1016/j.petrol.2016.02.011

33. Ellis, B. R., Fitts, J. P., Bromhal, G. S., McIntyre, D. L., Tappero, R., & Peters, C. A. (2013). Dissolution-driven permeability reduction of a fractured carbonate caprock. *Environmental Engineering Science*. https://doi.org/10.1089/ees.2012.0337

34. Beckingham, L. E. (2017). Evaluation of Macroscopic Porosity-Permeability Relationships in Heterogeneous Mineral Dissolution and Precipitation Scenarios. *Water Resources Research*, *53*(12). https://doi.org/10.1002/2017WR021306

35. Qin, F., & Beckingham, L. E. (2021). The impact of mineral reactive surface area variation on simulated mineral reactions and reaction rates. *Applied Geochemistry*, *124*. https://doi.org/10.1016/j.apgeochem.2020.104852

36. Beckingham, L. E., Steefel, C. I., Swift, A. M., Voltolini, M., Yang, L., Anovitz, L. M., Sheets, J. M., Cole, D. R., Kneafsey, T. J., Mitnick, E. H., Zhang, S., Landrot, G., Ajo-Franklin, J. B., DePaolo, D. J., Mito, S., & Xue, Z. (2017). Evaluation of accessible mineral surface areas for improved prediction of mineral reaction rates in porous media. *Geochimica et Cosmochimica Acta*, *205*. https://doi.org/10.1016/j.gca.2017.02.006

37. Qin, F., & Beckingham, L. E. (2019). Impact of image resolution on quantification of mineral abundances and accessible surface areas. *Chemical Geology*, *523*. https://doi.org/10.1016/j.chemgeo.2019.06.004

38. Landrot, G., Ajo-Franklin, J. B., Yang, L., Cabrini, S., & Steefel, C. I. (2012). Measurement of accessible reactive surface area in a sandstone, with application to CO 2 mineralization. *Chemical Geology*, *318–319*. https://doi.org/10.1016/j.chemgeo.2012.05.010

39. Peters, C. A. (2009). Accessibilities of reactive minerals in consolidated sedimentary rock: An imaging study of three sandstones. *Chemical Geology*, *265*(1–2). https://doi.org/10.1016/j.chemgeo.2008.11.014

40. Gringarten, E., & Deutsch, C. V. (2001). Teacher's aide: Variogram interpretation and modeling. *Mathematical Geology*, *33*(4). https://doi.org/10.1023/A:1011093014141

41. Bianchi, M., & Pedretti, D. (2017). Geological entropy and solute transport in heterogeneous porous media. *Water Resources Research*, *53*(6). https://doi.org/10.1002/2016WR020195

42. Bianchi, M., & Pedretti, D. (2018). An Entrogram-Based Approach to Describe Spatial Heterogeneity With Applications to Solute Transport in Porous Media. *Water Resources Research*, *54*(7). https://doi.org/10.1029/2018WR022827

43. Naimi, B., Skidmore, A. K., Groen, T. A., & Hamm, N. A. S. (2015). On uncertainty in species distribution modelling. In *ITC Dissertation* (Vol. 267, Issue August).

44. Berryman, J. G., & Blair, S. C. (1986). Use of digital image analysis to estimate fluid permeability of porous materials: Application of two-point correlation functions. *Journal of Applied Physics*, *60*(6). https://doi.org/10.1063/1.337245

45. Blair, S. C., Berge, P. A., & Berryman, J. G. (1996). Using two-point correlation functions to characterize microgeometry and estimate permeabilities of sandstones and porous glass. *Journal of Geophysical Research B: Solid Earth*, *101*(9). https://doi.org/10.1029/96jb00879

46. Anovitz, L. M., Beckingham, L. E., Sheets, J., Swift, A., Cole, D. R. (2021) A Novel Approach for the Analysis of Reactive Mineralogy and Surface Area. [Manuscript in progress]

Appendix A

Chapter 2: Role of mineralogy in controlling fracture formation
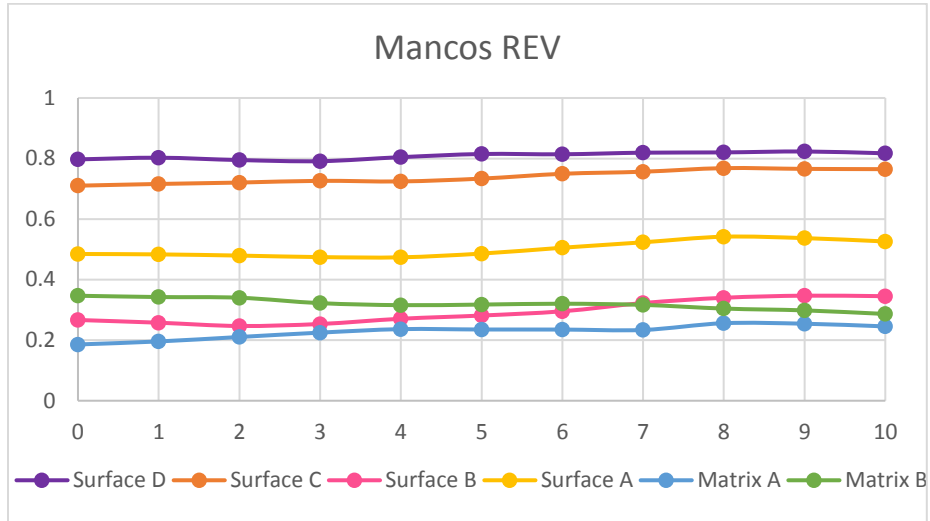
Figure A.1. REV check for Mancos SEM images where each step on the x-axis denotes a 10% decrease in image size, and the y-axis is the percentage of kaolinite left in the image.
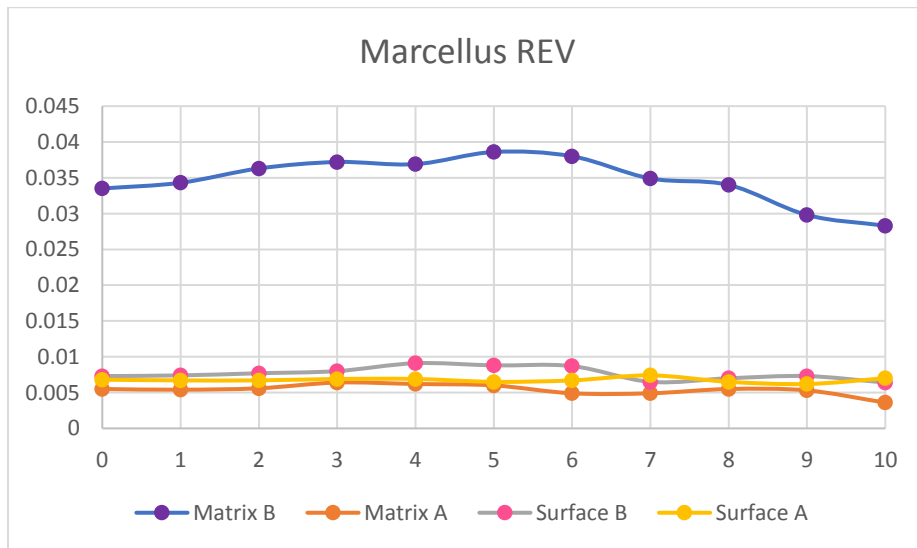

Figure A.2. REV check for Marcellus SEM images where each step on the x-axis denotes a 10% decrease in image size, and the y-axis is the percentage of quartz left in the image.
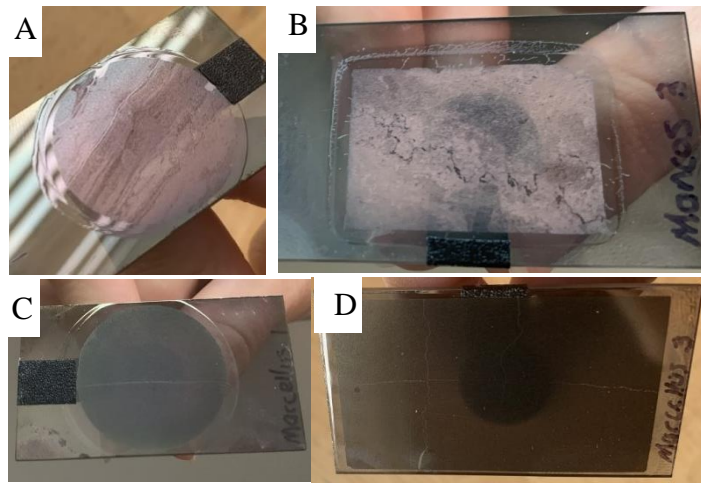
Figure A.3. Thin sections for imagining analysis of matrix. Mancos perpendicular (A) and parallel (B) to fracture. Marcellus perpendicular (C) and parallel (D) to fracture.

Chapter 3: Analysis of mineralogical spatial variation through autocorrelation
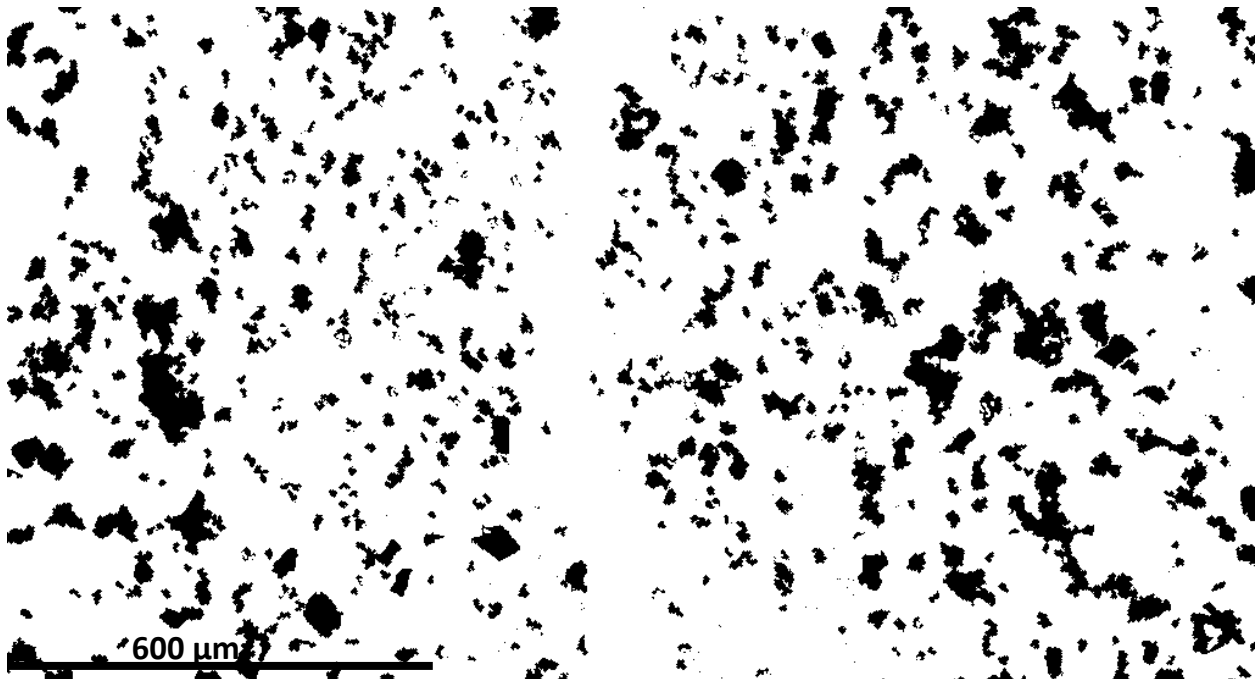
Figure B.1 Carbonate binary for cross-sectional Mancos matrix (Fig. 2.6A) where black is carbonate and white is everything else.
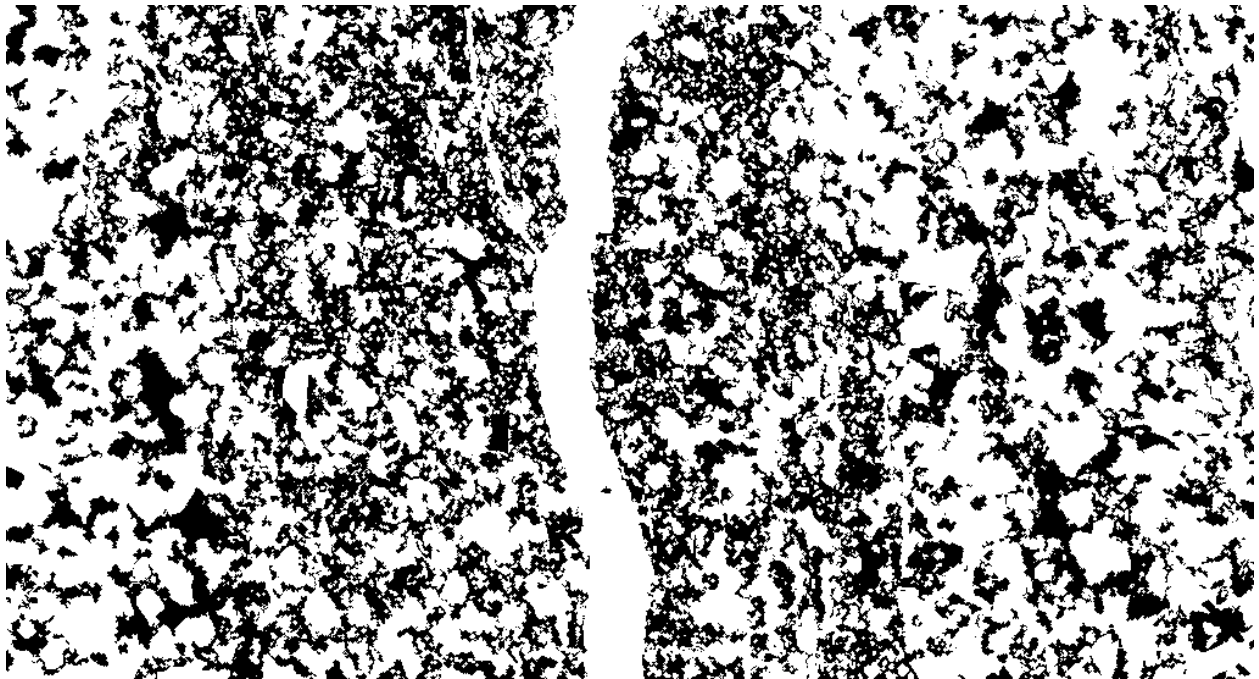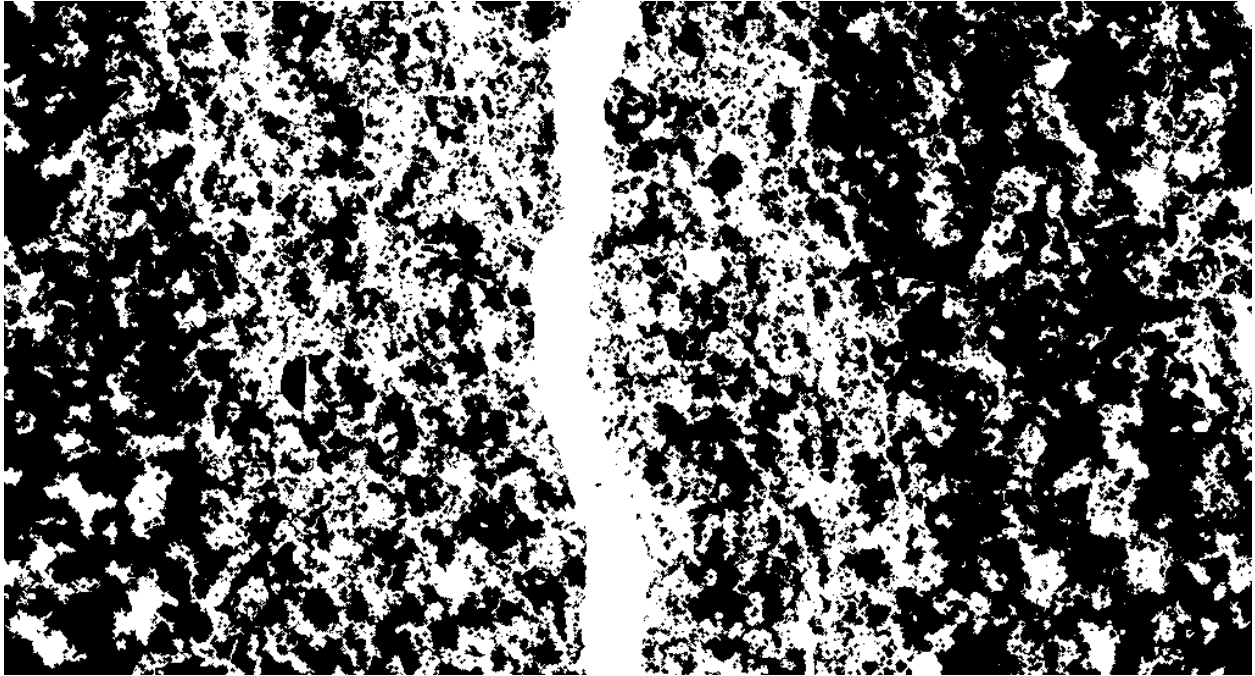

Figure B.2 Carbonate-clay binary for cross-sectional Mancos matrix (Fig. 2.6A) where black is carbonate and clay, and white is everything else.

Figure B.3 Carbonate-quartz binary for cross-sectional Mancos matrix (Fig. 2.6A) where black is carbonate and quartz, and white is everything else.

Figure B.4 Carbonate-pore binary for cross-sectional Mancos matrix (Fig. 2.6A) where black is carbonate and pore, and white is everything else.
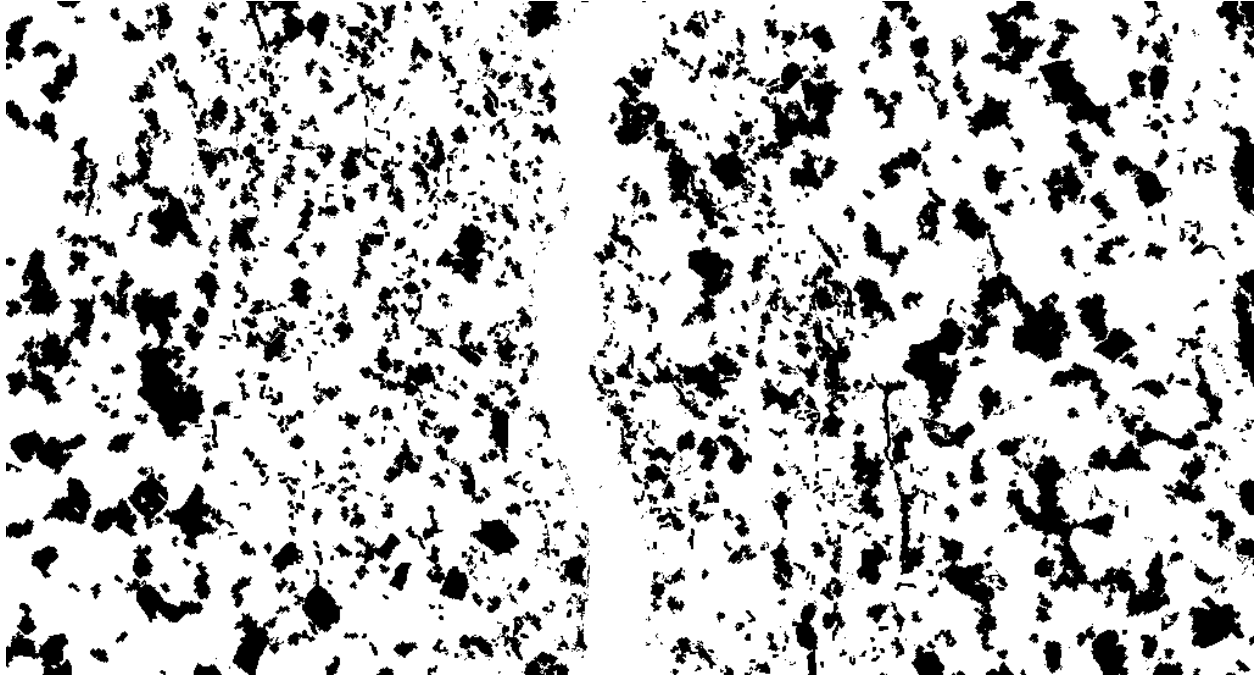
Figure B.5 Carbonate-other binary for cross-sectional Mancos matrix (Fig. 2.6A) where black is carbonate and other group, and white is everything else.
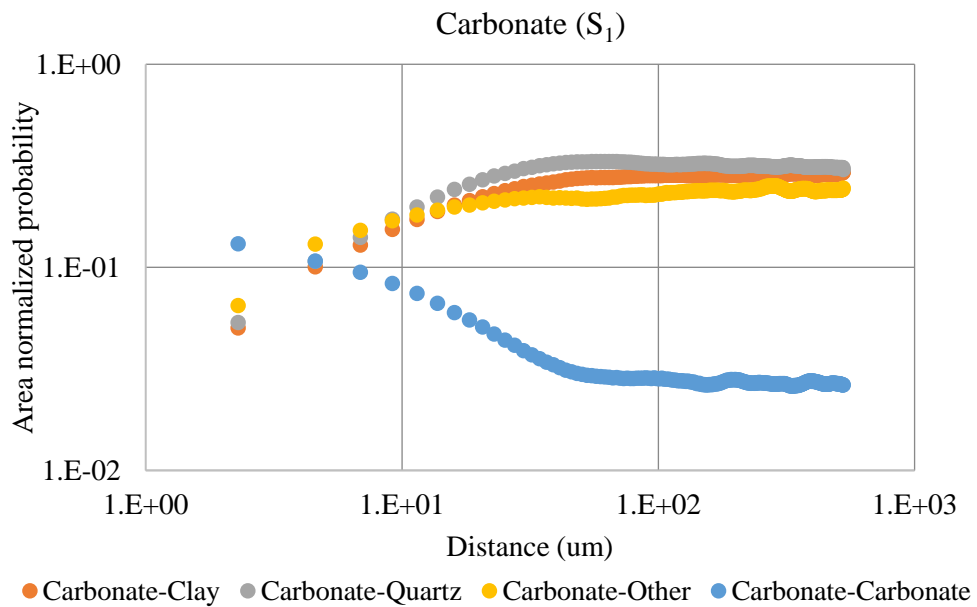

Figure B.6. Area normalized autocorrelation with respect to carbonate along the fracture (θ_1) in Figure 2.6A.
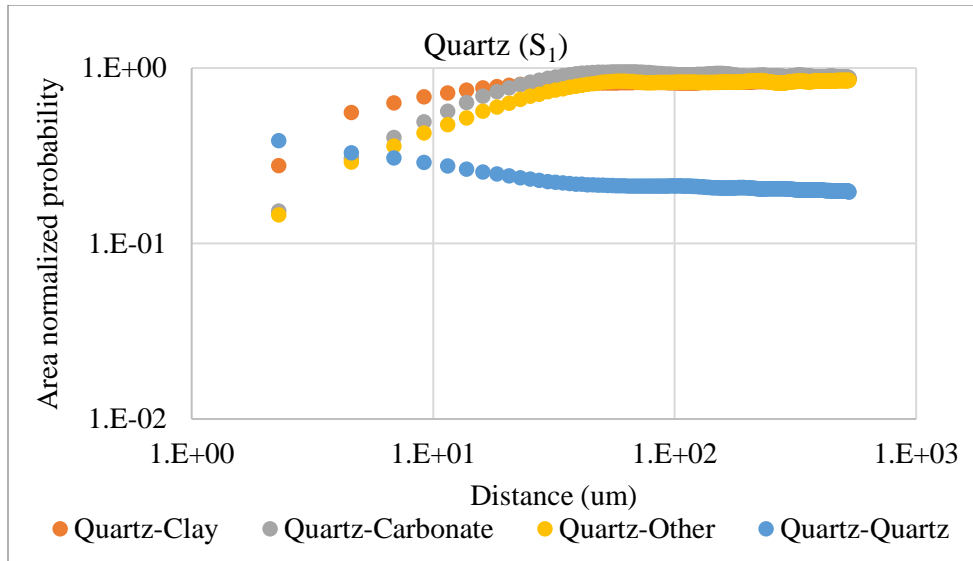
Figure B.7. Area normalized autocorrelation with respect to quartz along the fracture (θ_l) in Figure 2.6A.
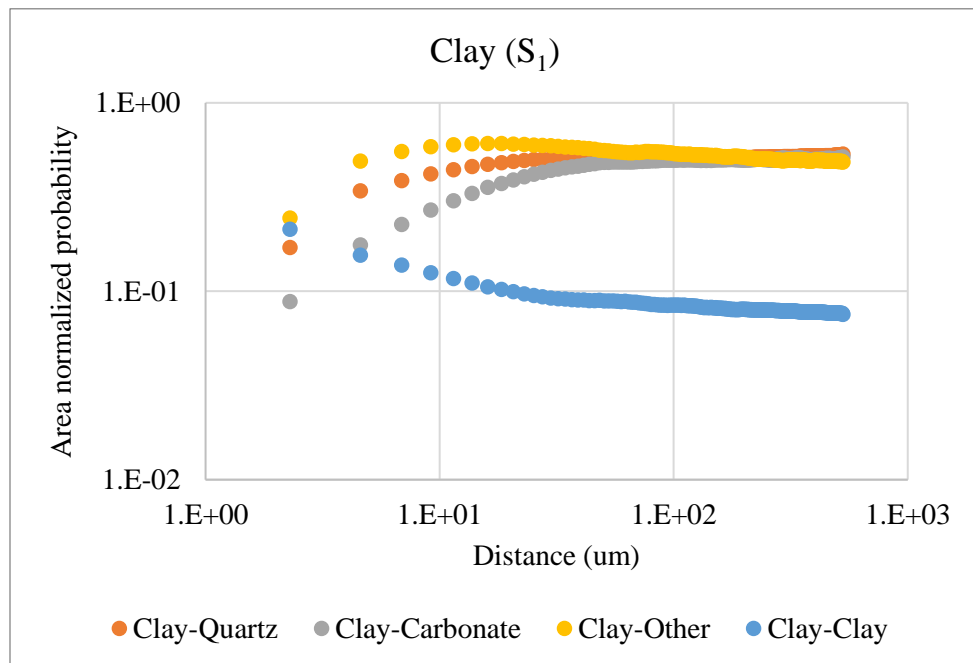

Figure B.8. Area normalized autocorrelation with respect to clay along the fracture (θ_l) in Figure 2.6A.